Agricultural and Forest Meteorology 171–172 (2013) 187–202

Contents lists available at SciVerse ScienceDirect

Agricultural and Forest Meteorology

journal homepage: www.elsevier.com/locate/agrformet

MODIS-driven estimation of terrestrial latent heat flux in China based on a modified Priestley–Taylor algorithm

Yunjun Yao[a,b,*], Shunlin Liang[a,b,c], Jie Cheng[a,b], Shaomin Liu[d], Joshua B. Fisher[e], Xudong Zhang[f], Kun Jia[a,b], Xiang Zhao[a,b], Qiming Qin[g], Bin Zhao[h], Shijie Han[i], Guangsheng Zhou[j], Guoyi Zhou[k], Yuelin Li[k], Shaohua Zhao[l]

[a] *State Key Laboratory of Remote Sensing Science, Jointly Sponsored by Beijing Normal University and Institute of Remote Sensing Applications, CAS, China*
[b] *College of Global Change and Earth System Science, Beijing Normal University, Beijing 100875, China*
[c] *Department of Geographical Sciences, University of Maryland, College Park, MD 20742, USA*
[d] *State Key Laboratory of Remote Sensing Science, School of Geography, Beijing Normal University, Beijing 100875, China*
[e] *Jet Propulsion Laboratory, California Institute of Technology, 4800 Oak Grove Dr., Pasadena, CA 91109, USA*
[f] *The Institute of Forestry, Chinese Academy of Forestry, Beijing 100091, China*
[g] *Institute of Remote Sensing and GIS, Peking University, Beijing 100871, China*
[h] *Ministry of Education Key Laboratory for Biodiversity Science and Ecological Engineering, Fudan University, Shanghai 200433, China*
[i] *Institute of Applied Ecology, Chinese Academy of Sciences, Shenyang 110016, China*
[j] *Laboratory of Quantitative Vegetation Ecology, Institute of Botany, Chinese Academy of Sciences, Beijing 100093, China*
[k] *South China Botanic Garden, Chinese Academy of Sciences, Guangzhou 510650, China*
[l] *Ministry of Environmental Protection, Environmental Satellite Center, Beijing 100094, China*

ARTICLE INFO

Article history:
Received 20 December 2011
Received in revised form
22 November 2012
Accepted 26 November 2012

Keywords:
Latent heat flux
Evapotranspiration
Priestley–Taylor
MODIS
China

ABSTRACT

Because of China's large size, satellite observations are necessary for estimation of the land surface latent heat flux (*LE*). We describe here a satellite-driven Priestley–Taylor (*PT*)-based algorithm constrained by the Normalized Difference Vegetation Index (*NDVI*) and Apparent Thermal Inertia (*ATI*) derived from temperature change over time. We compare to the satellite-driven *PT*-based approach, *PT-JPL*, and validate both models using data collected from 16 eddy covariance flux towers in China. Like *PT-JPL*, our proposed algorithm avoids the computational complexities of aerodynamic resistance parameters. We run the algorithms with monthly Moderate Resolution Imaging Spectroradiometer (*MODIS*) products (0.05° resolution), including albedo, Land Surface Temperature (*LST*), surface emissivity, and *NDVI*; and, Insolation from the Japan Aerospace Exploration Agency (*JAXA*). We find good agreement between our estimates of monthly *LE* and field-measured *LE*, with respective Root Mean Square Error (*RMSE*) and bias differences of 12.5 W m^{-2} and −6.4 W m^{-2}. As compared with *PT-JPL*, our proposed algorithm has higher correlations with ground-measurements. Between 2001 and 2010, *LE* shows generally negative trends in most regions of China, though positive *LE* trends occur over 39% of the region, primarily in Northeast, North and South China. Our results indicate that the variations of terrestrial *LE* are responding to large-scale droughts and afforestation caused by human activity with direct links to terrestrial energy exchange, both spatially and temporally.

1. Introduction

Latent heat flux (*LE*) and evapotranspiration (*ET*) link the water, carbon and energy cycles with *ET* absorbing more than half of total incoming terrestrial solar energy and returning more than 60% of land precipitation back to the atmosphere (L'vovich and White, 1990; Trenberth et al., 2009; Liang et al., 2010; Jung et al., 2010; Mu et al., 2011). In arid and semi-arid regions, such as those comprising a large portion of China, *ET* accounts for more than 70% of the annual water balance (Gao et al., 2007). Accurate and temporally continuous estimation of *LE* for China is critical for understanding the interactions between the land surface and atmosphere, and it is crucial for providing valuable means to efficient water resource use (Meyer, 1999; Raupach, 2001; Wang et al., 2012; Anderson et al., 2007; Yao et al., 2011a). Point *LE* observations are available from the ChinaFlux project, but do not cover the heterogeneity of landscapes and complexity of physical *ET* processes throughout China (Gash, 1987; Norman et al., 1995; Wang et al., 2010a,b).

* Corresponding author at: College of Global Change and Earth System Science, Beijing Normal University, Beijing 100875, China. Tel.: +86 10 5880 3002.
E-mail address: boyyunjun@163.com (Y. Yao).

0168-1923/$ – see front matter © 2012 Elsevier B.V. All rights reserved.
http://dx.doi.org/10.1016/j.agrformet.2012.11.016

Remote sensing has greatly improved large scale observation of soil and vegetation dynamics, and has played an increasingly important role in estimation of *LE* over heterogeneous landscapes (Zhang et al., 2008; Wang et al., 2010a,b,c). Inputs for remotely sensed *LE* estimates generally consist of albedo, land surface temperature (*LST*), leaf area index (*LAI*), vegetation indices (*VI*) and other meteorological ground observations. In the last two decades, several satellite-based *LE* approaches have become available for determining different scale *LE*, including (1) empirical and semi-empirical methods (Jackson et al., 1977; Wang et al., 2007; Mueller et al., 2011; Jin et al., 2011; Jung et al., 2010), (2) surface energy balance models (*SEB*) (Norman et al., 1995; Kustas and Norman, 1996), (3) Penman–Monteith (*PM*)-based (Monteith, 1965) approaches (Mu et al., 2007) and (4) Priestley–Taylor (*PT*)-based (Priestley and Taylor, 1972) approaches (Fisher et al., 2008). Empirical and semi-empirical methods have been designed based on the statistical relationships between ground-measured *LE* and a suite of eco-environmental parameters derived from satellite and ground observations (Jin et al., 2011). Although empirical methods are easy to operate for mapping long-term *ET* in large-scale applications, the empirical coefficients may vary from the different ecosystems and require further calibration.

Surface energy balance *LE* methods are developed from the surface energy budget. Among such models, One-source Surface Energy Balance (*SEB*) (Monteith, 1965), Two-source Surface Energy Balance (*TSEB*) (Shuttleworth and Wallace, 1985), the Atmosphere–Land Exchange Inverse (*ALEXI*) model (Anderson et al., 1997) and the Surface Energy Balance Algorithm for Land (*SEBAL*) (Bastiaanssen et al., 1998) all perform reasonably well for point *LE* or *ET* estimation. However, a longstanding limitation associated with these methods is that their aerodynamic and surface resistances rely on some important variables, such as wind speed or vapor pressure deficit (*VPD*), that are usually not available from remote sensing data (Yao et al., 2011b).

To overcome the problems in the *SEB* models, Cleugh et al. (2007) developed a remotely sensed *LE* model using a *PM* equation driven by *MODIS*-derived vegetation data and daily surface meteorological inputs. Subsequently, Mu et al. (2007) and Zhang et al. (2009) further modified Cleugh et al.'s model to estimate the global *ET* (*RS-ET*) based on *LAI* and *NDVI* retrieved from remote sensing data. Currently, although the *PM* method can successfully produce *MODIS ET* products (Mu et al., 2011: MOD16), many parameters for calculating canopy and aerodynamic resistances still depend on ground meteorological observations and reanalysis products.

The Priestley–Taylor equation can be considered a simplified version of the more theoretical Penman equation that avoids the calculation of the aerodynamic and surface resistance (Priestley and Taylor, 1972; Fisher et al., 2008; Jin et al., 2011; Miralles et al., 2011). Inputs for the *PT* equation include net radiation, ground heat flux, and air temperature. A coefficient multiplier, alpha, sets the equation equal to potential *ET*; some authors have changed the value of alpha in an attempt to reduce potential *ET* to actual *ET*. Accurate parameterization of this parameter is difficult because it varies from 0 (dry surface) to approximately 1.26 (wet surface) in different regions and times of the year/day (Sumner and Jacobs, 2005). The Priestley–Taylor coefficient has been modified using the two-step interpolation scheme from the dry and wet edges in the *LST-NDVI* triangular space (Jiang and Islam, 2001; Tang et al., 2010), ecophysiological constraints (Norman et al., 1995; Fisher et al., 2008; Jin et al., 2011) or the parameterization of microwave-derived soil moisture (Miralles et al., 2011). However, few of these approaches couple canopy interception evaporation with soil moisture conditions, so parameterization schemes still need many variables, such as relative humidity, soil moisture or precipitation, to improve the complexity of the models, and accumulated errors from too many input variables magnify the uncertainty of *ET* estimations.

In this study, to circumvent the difficulty of the satellite-based estimation of relative humidity (*RHD*) and vapor pressure deficit (*VPD*) for *PT-JPL* algorithm, we used the Apparent Thermal Inertia (*ATI*) derived from the temperature (air temperature, T_a, or land surface temperature, *LST*) change over time to replace *RHD* and *VPD* for calculating the soil moisture constraint. Our proposed algorithm only needs four variables, as follows: net radiation (R_n), air temperature (T_a), diurnal temperature range (*DT*) and *NDVI*. Next, we validated our method using ground-observed flux data from 16 flux towers in China and compared our method with the *PT-JPL* model (Fisher et al., 2008). Finally, we estimated the monthly *LE* in China driven by *MODIS* products and analyzed the variations of the terrestrial *LE* between 2001 and 2010.

2. Method and data

2.1. Description of Priestley–Taylor LE algorithm

To overcome the uncertainty of the resistances in the Penman–Monteith equation, Priestley and Taylor (1972) designed a simple *LE* equation for radiation- and temperature-based equilibrium evaporation by replacing the atmospheric demand with an empirical coefficient (α):

$$LE = \alpha \frac{\Delta}{\Delta + \gamma}(R_n - G) \quad (1)$$

where *LE* is the latent heat flux from the evapotranspiration process in W m^{-2}, α is the *PT* coefficient of 1.26 for a water body, Δ is the slope of the saturated vapor pressure curve (kPa °C^{-1}), and γ is the psychrometric constant (kPa °C^{-1}). R_n and G represent the net radiation and the soil heat flux in W m^{-2}, which can be estimated using satellite data and meteorological observations. In this paper, we have calculated water evaporation using Eq. (1). Fisher et al. (2008) developed a new method for downscaling potential *LE* from Priestley–Taylor to actual *LE* based on ecophysiological constraint functions driven by atmospheric moisture (*VPD* and *RHD*) and vegetation indices (normalized and soil adjusted vegetation indices, *NDVI* and *SAVI*). The *PT-JPL* algorithm can be described as:

$$LE = LE_s + LE_c + LE_i \quad (2)$$

$$LE_s = [f_{wet} + (1 - f_{wet})f_{sm}]\alpha \frac{\Delta}{\Delta + \gamma}(R_{ns} - G) \quad (3)$$

$$LE_c = (1 - f_{wet})f_c f_T f_M \alpha \frac{\Delta}{\Delta + \gamma} R_{nc} \quad (4)$$

$$LE_i = f_{wet}\alpha \frac{\Delta}{\Delta + \gamma} R_{nc} \quad (5)$$

where f_c is the green canopy fraction (f_{APAR}/f_{IPAR}), f_T is a plant temperature constraint ($\exp(-((T_{\max} - T_{opt})/T_{opt})^2)$), f_M is a plant moisture constraint ($f_{APAR}/f_{APAR_{\max}}$), f_{sm} is a soil moisture constraint (RHD^{VPD}) and f_{wet} is the relative surface wetness (RHD^4), f_{APAR} is the absorbed photosynthetically active radiation (*FPAR*), f_{IPAR} is the intercepted *PAR*, $T_{\max}$ is the maximum air temperature and T_{opt} is $T_{\max}$ at max ($R_n T_{\max} SAVI/VPD$).

2.2. Modified satellite-based Priestley–Taylor LE model

Taken interception into account is crucial when making *LE* estimates over large land masses because interception loss can be responsible for the evaporation of approximately 13–22% of the total *LE* in different forest biomes (Miralles et al., 2010). In our model, the total latent heat flux, *LE*, is calculated as the sum of the soil evaporation, the canopy transpiration, the wet soil surface evaporation and the canopy interception evaporation (Table 1).

Table 1
Model parameters and equations for the modified satellite-based Priestley–Taylor *LE* model. Δ is the slope of the saturate vapor pressure curve, γ is the psychrometric constant (0.066 kPa °C^{-1}), α = 1.26 (Priestley and Taylor, 1972), T_{opt} = 25 °C (Fisher et al., 2008; Yuan et al., 2010), a_g = 0.18 (Rouse, 1984; Halliwell and Rouse, 1987), $NDVI_{max}$ = 0.95 (Zhang et al., 2009), $NDVI_{min}$ = 0.05 (Zhang et al., 2009), $DTaR_{max}$ = 40 °C (this study), $DTsR_{max}$ = 60 °C (this study). For water body, $G = 0.26R_n$ (Zhang et al., 2009).

Parameter	Description	Equation	Reference
LE	Latent heat flux	$LE_s + LE_c + LE_{ic} + LE_{ws}$	
LE_c	Vegetation transpiration	$(1 - f_{wet})f_v f_T \alpha \frac{\Delta}{\Delta+\gamma} R_{nc}$	This study; Priestley and Taylor, 1972; Norman et al., 1995; Fisher et al., 2008
LE_s	Soil evaporation	$(1 - f_{wet})f_{sm} \alpha \frac{\Delta}{\Delta+\gamma}(R_{ns} - G)$	This study; Priestley and Taylor, 1972; Fisher et al., 2008
LE_{ic}	Vegetation interception evaporation	$f_{wet} \alpha \frac{\Delta}{\Delta+\gamma} R_{nc}$	This study; Fisher et al., 2008
LE_{ws}	Wet soil surface evaporation	$f_{wet} \alpha \frac{\Delta}{\Delta+\gamma}(R_{ns} - G)$	This study; Fisher et al., 2008
f_v	Fraction of green vegetation in the scene	$\frac{NDVI - NDVI_{min}}{NDVI_{max} - NDVI_{min}}$	This study; Zhang et al., 2009
f_T	Plant temperature constraint	$\exp\left[-\left(\frac{T_a - T_{opt}}{T_{opt}}\right)^2\right]$	This study; Fisher et al., 2008; Yuan et al., 2010
f_{sm}	Soil moisture constraint	$\left(\frac{1}{DT}\right)^{DT/DT_{max}}$	This study
f_{wet}	Relative surface wetness	f_{sm}^4	This study; Fisher et al., 2008
G	Soil heat flux	$a_g R_n(1 - f_v)$	This study; Rouse, 1984; Halliwell and Rouse, 1987
R_{nc}	Net radiation to the vegetation	$R_n f_v$	This study; Mu et al., 2007, 2011
R_{ns}	Net radiation to the soil	$R_n(1 - f_v)$	This study; Mu et al., 2007, 2011

Our algorithm is driven by four variables: net radiation (R_n), air temperature (T_a), diurnal temperature range (DT) and *NDVI*.

Soil evaporation (LE_s) follows *PT-JPL* and can be expressed as the following equation without interception evaporation.

$$LE_s = f_{sm}\alpha\frac{\Delta}{\Delta+\gamma}(R_{ns} - G) \quad (6)$$

In the above equation, an index of soil water deficit, f_{sm}, has been designed to constrain LE_s based on the complementary hypothesis of Bouchet (1963) whereby surface moisture status is linked to the evaporative demand of the atmosphere (Fisher et al., 2008). The surface tends to be in equilibrium with the overlying atmosphere and f_{sm} is a good indicator of soil moisture over large enough spatial and temporal scales. Generally soil moisture is reflected in the variation of Apparent Thermal Inertia (*ATI*) and *ATI* relates the diurnal temperature range (*DT*) (Price, 1985; Zhang et al., 2003; Wang and Liang, 2008). Thereby, it is possible to quantify f_{sm} using an exponential algorithm of *ATI* and f_{sm} can be calculated from the following equation:

$$f_{sm} = ATI^k = \left(\frac{1}{DT}\right)^{DT/DT_{max}} \quad (7)$$

where *DT* is the diurnal temperature range and *ATI* is the Apparent Thermal Inertia, which can be simplified as the inverted diurnal temperature range (*DT*) (diurnal land surface temperature range, $DTsR = LST_{day} - LST_{night}$ or diurnal air temperature range, $DTaR = T_{max} - T_{min}$. Using *DTsR* and *DTaR* as inputs for our modified *LE* model, hereafter called *PT-DTsR* and *PT-DTaR*, respectively) (Wang and Liang, 2008; Zhang et al., 2003; Seneviratne et al., 2010). Using the simplified *ATI* (1/*DT*) alone assumes a linear relationship with f_{sm}, and our initial inspection indicates lower-than-expected f_{sm} at high *DT* and higher-than-expected f_{sm} at low *DT*. Therefore, DT/DT_{max} has been selected as a k value to parameterize f_{sm}. DT_{max}, defining the relative sensitivity to the variation of *DT*, is the maximum diurnal temperature range and is set as invariant constants ($DTaR_{max}$ = 40 °C, $DTsR_{max}$ = 60 °C) in this paper. Given that f_{sm} is an index scaled between 0 and 1, we scale soil volumetric water (*VWC*, m^3 m^{-3}) between 0 and 1 for validation and comparison. Thus relative extractable water (*REW*, $REW = (VWC - VWC_{min})/(VWC_{max} - VWC_{min})$) can be derived from ground-based *VWC* (Fisher et al., 2008; Anderson et al., 2007). Fig. 1 shows the variation plot between f_{sm} and *REW* from 0 to 20 mean soil moisture at both the Shapotou (desert) flux tower and the Dinghushan (forest) flux tower, which indicates that the f_{sm} closely follows *REW*.

For vegetation transpiration (LE_c), we use the modified Linear Two-Source Model (*N95*) to estimate vegetation transpiration (Norman et al., 1995; Anderson et al., 1997; Fisher et al., 2008). Assuming no canopy interception, the algorithm of vegetation transpiration can be described as:

$$LE_c = f_v f_T \alpha \frac{\Delta}{\Delta+\gamma} R_{nc} \quad (8)$$

where f_v refers to the fraction of green vegetation in the scene and it characterizes the variations of surface vegetation transpiration amount because vegetation transpiration couples with CO_2 assimilation through the process of vegetation photosynthesis (Tucker, 1979; Norman et al., 1995; Wang et al., 2007). f_v has been estimated as a linear function of *NDVI* considering *NDVI*, determined by the seasonal dynamics of vegetation, represents the variations in vegetation state and canopy response to changes in environmental conditions such as the plant water potential, *FPAR* and CO_2 concentration (Tucker, 1979; Zhang et al., 2010). Additionally, we have added the temperature constraint, f_T, with an optimum T_{opt} set at 25.0 °C, rather than dynamically calculated as in *PT-JPL* (Fisher et al., 2008; Yuan et al., 2010). Another difference between our modified vegetation transpiration algorithm and *N95* model is that

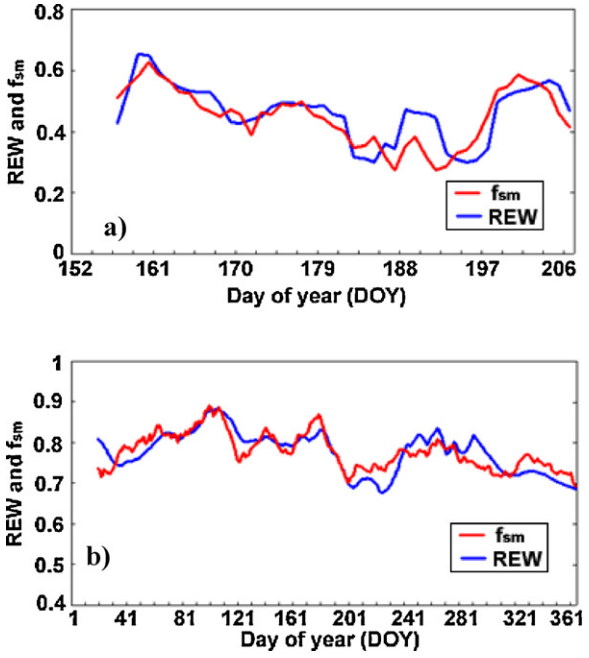

Fig. 1. Comparisons of the smoothed f_{sm} and relative extractable water (*REW*) from 0 to 20 mean soil moisture at (a) Shapotou (desert) flux tower, and (b) Dinghushan (forest) flux tower.

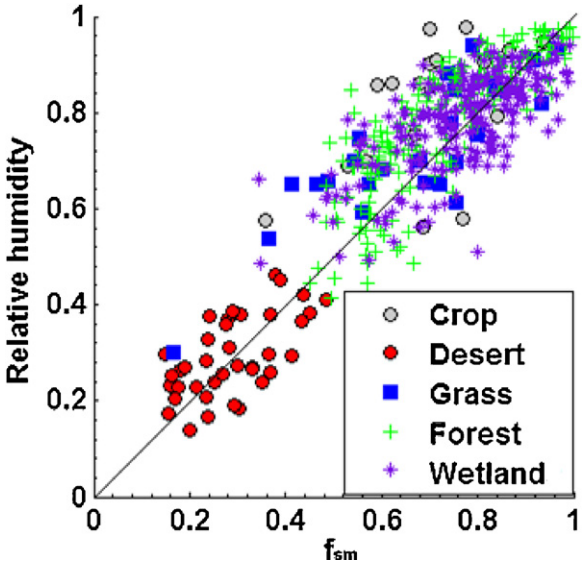

Fig. 2. The scatter plot between relative humidity (*RHD*) and f_{sm} at 5 different biome types (R^2 = 0.75).

the coefficient of Priestley–Taylor (α) of Eq. (8) is set as the invariant constant 1.26 rather than 1.3 to keep the consistency with the original Priestley–Taylor model.

For canopy interception evaporation (LE_{ic}), we follow *PT-JPL*, but replace f_{wet} with f_{sm}^4 due to the good agreement between f_{sm} and relative humidity at 5 different biome types of China (daily, $R^2 \sim 0.75$, Fig. 2). Similarly, the wet soil surface evaporation (LE_{ws}) can also be calculated based on f_{sm}^4. The detailed description of the modified Priestley–Taylor model is shown in Table 1.

2.3. MODIS-based air temperature estimate

Air temperature is one of the core inputs for almost all *LE* models. However, the density of the meteorological network is often too sparse and cannot provide a spatially distributed characterization (Zakšek and Homscheidt, 2009). Remote sensing detects thermal signals, including a mixture of land surface signals and air signals. Thus, air temperature can be derived from *LST* by correlating the daily or monthly mean air temperature measured at meteorological stations, with *LST* obtained from remote sensing (Sun et al., 2005). The presented satellite-derived air temperature methods have an inherent error of up to approximately 2 °C, with either a high temporal or a high spatial resolution. In this study, we have established a simple statistical approach based on a linear regression between the observed air temperature and two surface variables (*LST* and *NDVI*) to estimate the monthly air temperature in China from *MODIS* products.

$$T_a = a_0 + a_1 T_s + a_2 NDVI \tag{9}$$

$$T_s = \frac{LST_{day} + LST_{night}}{2} \tag{10}$$

a_i (i = 0, 1, 2) is the coefficient, which can be calibrated by linear regression using the observed monthly air temperature data for 2001–2005 from all 752 meteorological stations in China and the monthly *MODIS* products (*LST* and *NDVI*). The *NDVI* can be obtained from monthly *MODIS NDVI* products from 2001 through 2010 at a 0.05° spatial resolution. Quality control (*QC*) flags are examined to screen and reject *NDVI* data of insufficient quality (other parameters, such as *LST*, albedo, from *MODIS* are all processed using the same procedure).

T_a is the monthly air temperature (°C). T_s is the mean monthly land surface temperature(°C), which can be estimated by averaging two-phase data through two *MODIS* Terra temperatures at 0.05° spatial resolution. *MODIS* Terra makes two monthly observations, one during the daytime (LST_{day}) and the second at night (LST_{night}).

2.4. Regional net radiation estimate

The surface net radiation (R_n) is the sum of the incidents of downward and upward shortwave and longwave radiation. In this paper, R_n can be calculated from the following equation:

$$R_n = S_{\downarrow}(1 - A) + \varepsilon_s L_{\downarrow} - L_{\uparrow} \tag{11}$$

where $S_{\downarrow}$ is the surface downward shortwave radiation (*Insolation*) (W m^{-2}). We use the monthly *Insolation* products (*MOD02SSH*) from January to December for 2001–2010 at a spatial resolution of 0.05°, which is derived from the *MODIS Insolation* products produced by Japan Aerospace Exploration Agency (*JAXA*). The parameter A is the surface albedo, and we have derived all the sky shortwave albedo monthly based on the *MODIS* collection 5 surface Bidirectional Reflectance Distribution Function (*BRDF*)/albedo product at a 0.05° spatial resolution. The actual surface albedo is

Table 2
Locations of the 16 flux towers used in this study.

Name	Lat, Lon	Land cover	Elevation (m)	Mean ET (W m^{-2})	Mean NDVI	Measurement method	Project	Time period
Dongsu (DS), Inner Mongolia	44.09°N, 113.57°E	Desert steppe	970	34.7	0.22	ECOR	CEOP	2008 (Jul–Sep)
Jinzhou (JZ), Liaoning	41.18°N, 121.21°E	Crop(maize)	22.3	89.6	0.71	ECOR	CEOP	2008 (Jul–Sep)
Miyun (MY), Beijing	40.63°N, 117.32°E	Mixture	350	102.9	0.72	ECOR	CEOP	2008 (Jul–Sep)
Shouxian (SX), Anhui	32.56°N, 116.78°E	Mixture	22.7	61.6	0.53	ECOR	ARM	2008 (May–Dec)
Tongyu (TY), Jilin	44.57°N, 122.88°E	Pasture	184	54.1	0.46	ECOR	CEOP	2008 (Jul–Sep)
Guantao (GT), Hebei	36.52°N, 115.13°E	Crop(wheat)	42	82.4	0.65	ECOR	CEOP	2009 (Jun–Sep)
Qingyang (QY), Gansu	35.59°N, 107.54°E	Grass	1095	51.8	0.45	ECOR	CEOP	2009 (Jul–Sep)
Shapotou (SPT), Ningxia	37.53°N, 105.18°E	Desert	1227	36.9	0.17	ECOR	CEOP	2009 (Jun–Sep)
Laoshan (LS), Heilongjiang	45.28°N, 127.58°E	Larch forest	340	31.9	0.46	ECOR	ChinaFlux	2002 (May–Dec)
Dinghushan (DHS), Guangdong	23.17°N, 112.54°E	Coniferous broadleaf mixed forest	240	69.1	0.68	ECOR	ChinaFlux	2003 (Jan–Dec)
Yueyang (YY), Hunan	29.31°N, 112.51°E	Deciduous broadleaf forests	31	67.2	0.54	ECOR	ChinaFlux	2005 (Jan–Dec)
Xilinhot (XLH), Inner Mongolia	44.13°N, 116.33°E	Typical steppe	1187	15.8	0.26	ECOR	ChinaFlux	2005 (Jan–Dec)
Changbaishan (CBS), Jilin	42.40°N, 128.10°E	Mixed forests	761	41.5	0.38	ECOR	ChinaFlux	2003 (Jan–Dec)
Dongtan (DT), Shanghai	31.58°N, 121.90°E	Permanent wetland	5	55.8	0.12	ECOR	ChinaFlux	2005 (Jan–Dec)
Haibei (QHB), Qinghai	37.60°N, 101.33°E	Alpine meadow	3250	37.1	0.39	ECOR	ChinaFlux	2003 (Jan–Dec)
Zhangye (ZY), Gansu	39.09°N, 100.30°E	Steppe desert	1483	29.1	0.48	ECOR	CEOP	2008 (Jul–Sep)

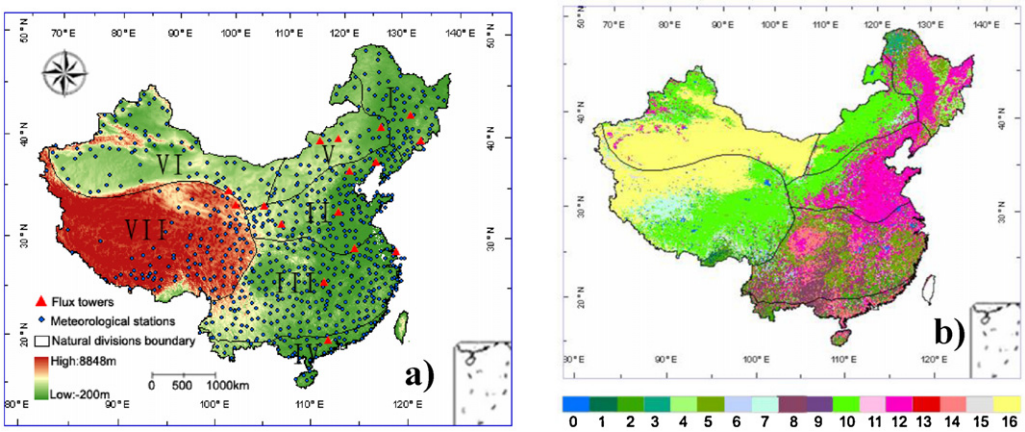

Fig. 3. Locations of the study area and land cover classification. (a) Locations of 16 flux towers, 752 meteorological stations and 7 natural divisions throughout China. Natural divisions are shown: I, Northeast China; II, North China; III, Central China; IV, South China; V, Inner Mongolia; VI, Northwest China; and VII, Qinghai-Tibet region. (b) Land cover classification of China used in this study. IGBP land cover types are shown: 0, water body; 1, evergreen needleleaf forest; 2, evergreen broadleaf forest; 3, deciduous needleleaf forest; 4, deciduous broadleaf forest; 5, mixed forest; 6, closed shrubland; 7, open shrubland; 8, woody savanna; 9, savanna; 10, grassland; 11, permanent wetland; 12, crop land; 13, urban/build up; 14, crop land/natural vegetation mosaic; 15, snow/ice; and 16, barren lands.

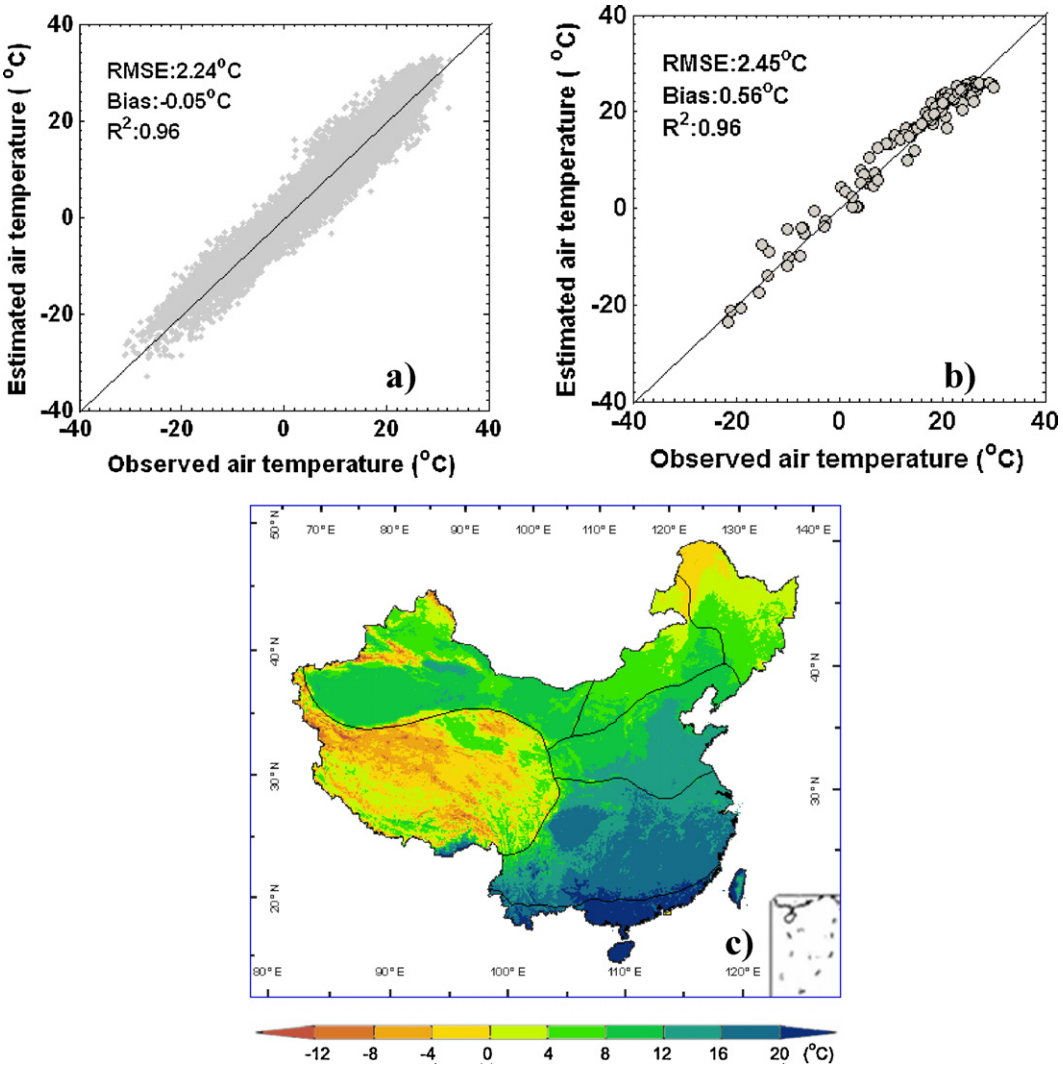

Fig. 4. (a) The comparison of the monthly estimated air temperature using Eq. (21) from 0.05 *MODIS* products and observed air temperature at 752 meteorological stations in mainland China. (b) Independent validation of the monthly estimated air temperature using Eq. (21) from *MODIS* products at 0.05° and observed air temperature at 16 flux towers. (c) Map of annual air temperature (°C) for 2001 based on Eq. (21) from monthly *MODIS* averaged *LST* and *NDVI* products.

obtained by adding 50% of the black-sky albedo and 50% of the white-sky albedo. ε_s is the surface emissivity. The unreliable or missing albedo data are also temporally filled using the method proposed by Zhao et al. (2005). $L_\downarrow$ and $L_\uparrow$ are the downward and upward long wave radiation flux (W m^{-2}), respectively. ε_s can be calculated by the following equation (Wang et al., 2005):

$$\varepsilon_s = 0.2122\varepsilon_{29} + 0.3859\varepsilon_{31} + 0.4029\varepsilon_{32} \quad (12)$$

where ε_{29}, ε_{31} and ε_{32} are the emissivities in MODIS bands 29, 31 and 32, respectively, which are part of the monthly *LST* products at 0.05° spatial resolution.

$L_\downarrow$ and $L_\uparrow$ can be estimated by the equations (Jacobs, 1978):

$$L_\downarrow = (1 + 0.26n)L_{\downarrow\, clear} \quad (13)$$

$$L_{\downarrow\, clear} = \varepsilon_a \sigma (T_a + 273.15)^4 \quad (14)$$

$$L_\uparrow = \varepsilon_s \sigma (T_s + 273.15)^4 \quad (15)$$

where ε_a is the atmospheric emissivity; σ is the Stefan–Boltzman constant (5.67×10^{-8} W m^{-1} K^{-4}); n is the cloudiness varying from 0 to 1 and is set as invariant constants (0.5) in this paper; ε_a can be calculated from T_a (°C) using the following formula (Idso and Jackson, 1969):

$$\varepsilon_a = 1 - 0.261 \times \exp[-7.77 \times 10^{-4} \times (T_a + 0.15)^2] \quad (16)$$

In addition to the *MODIS* products, we also use monthly Palmer Drought Severity Index (*PDSI*) products derived from the *NCAR* CGD's Climate Analysis Section dataset, with a 2.5° spatial resolution, for the period from 2001 through 2010. To highlight the obvious spatial variation features of both *LE* and *PDSI*, we have interpolated the *PDSI* products into 0.05° from a 2.5° spatial resolution.

2.5. Validation data

Ground-measured latent heat flux (*LE*), sensible heat flux (*H*), air temperature (T_a), vapor pressure (e), relative humidity (*RHD*), diurnal temperature range (*DT*), ground heat flux (G) and net radiation (R_n) are collected from the 8 flux towers under a Coordinated Enhanced Observation Project (*CEOP*) in the arid and semi-arid regions of northern China, 1 flux tower of Atmosphere Radiation Measurement (*ARM*) in South Central China, and 7 flux towers of *ChinaFlux* in both Southeast and Northeast China (Table 2). The land cover types of the flux towers include crop fields, grass, steppe, pastures, desert, wetland, forests and mixed cover, including vegetation and bare soil at vastly different locations (Table 2 and Fig. 3). All the radiation flux experiments are conducted based on the eddy covariance (*ECOR*) method and *ECOR* suffers from an energy imbalance problem (Jung et al., 2010). Therefore, the method put forward by Twine et al. (2000) has been selected to correct the *LE* obtained from different towers (except for the Yueyang site because of the deficiency of the measured *H*), and the corrected method is as follows:

$$LE = \frac{LE_{EC}}{R_c} \quad (17)$$

$$R_c = \frac{LE_{EC} + H_{EC}}{R_n - G} \quad (18)$$

Here, *LE* is the corrected latent heat flux. R_c is the energy closure ratio. LE_{EC} and H_{EC} are the original latent heat flux and the sensible heat flux measured by the *ECOR* method, respectively.

MODIS NDVI composite products (*MOD13A2*) with a 1-km spatial resolution and a 16-day temporal resolution are used to validate different *LE* algorithms in this paper, and the daily *NDVI* values are temporally interpolated from the 16-day averages using linear interpolation. Similarly, *MODIS FPAR* composite products (*MOD15A2*) with a 1-km spatial resolution and an 8-day temporal resolution are also used to validate the *PT-JPL* model. Both the daily daytime *LST* and the night time *LST* under clear skies are extracted from the daily *MODIS LST* products (*MOD11A1*) with a 1-km spatial resolution. The water surfaces are identified using the *MODIS*-based International Geosphere-Biosphere Programme (*IGBP*) land cover types from *MOD12* products for the year 2004 at 0.05° spatial resolution, assuming that there is no change in the water body information during this decade (Fig. 3).

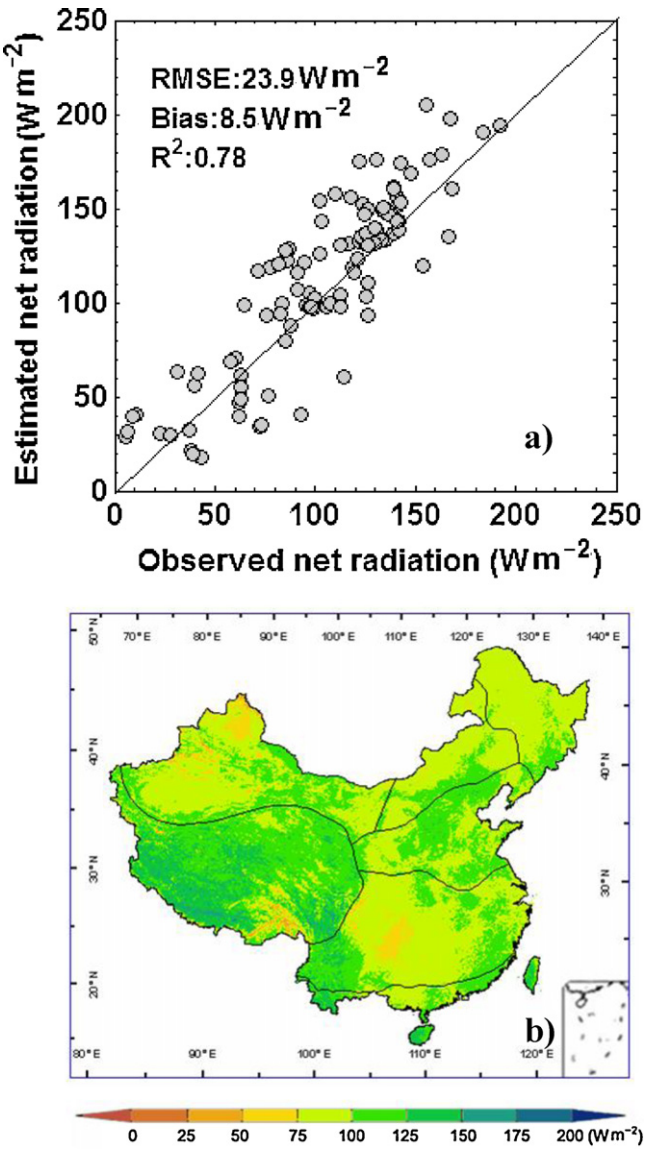

Fig. 5. (a) Independent validation of the monthly estimated net radiation from *MODIS* products at 0.05° and observed net radiation at 16 flux towers. (b) Map of annual net radiation (W m^{-2}) for 2001 based on Eq. (11) from monthly *MODIS* products.

2.6. Model performance and trend analysis

For model validation and trend analysis, we analyze the correlation and p values of the modeled *LE* and those derived from the tower data, as well as the correlation, root mean square error (*RMSE*), and mean bias to quantify how closely the modeled *LE* resembles the observed *LE*. Linear trend analysis is used to analyze the regional trends of the *LE* variables (y_t). The linear model is used to simulate y_t against time (t).

$$y_t = y_0 + bt + \varepsilon_t \quad (19)$$

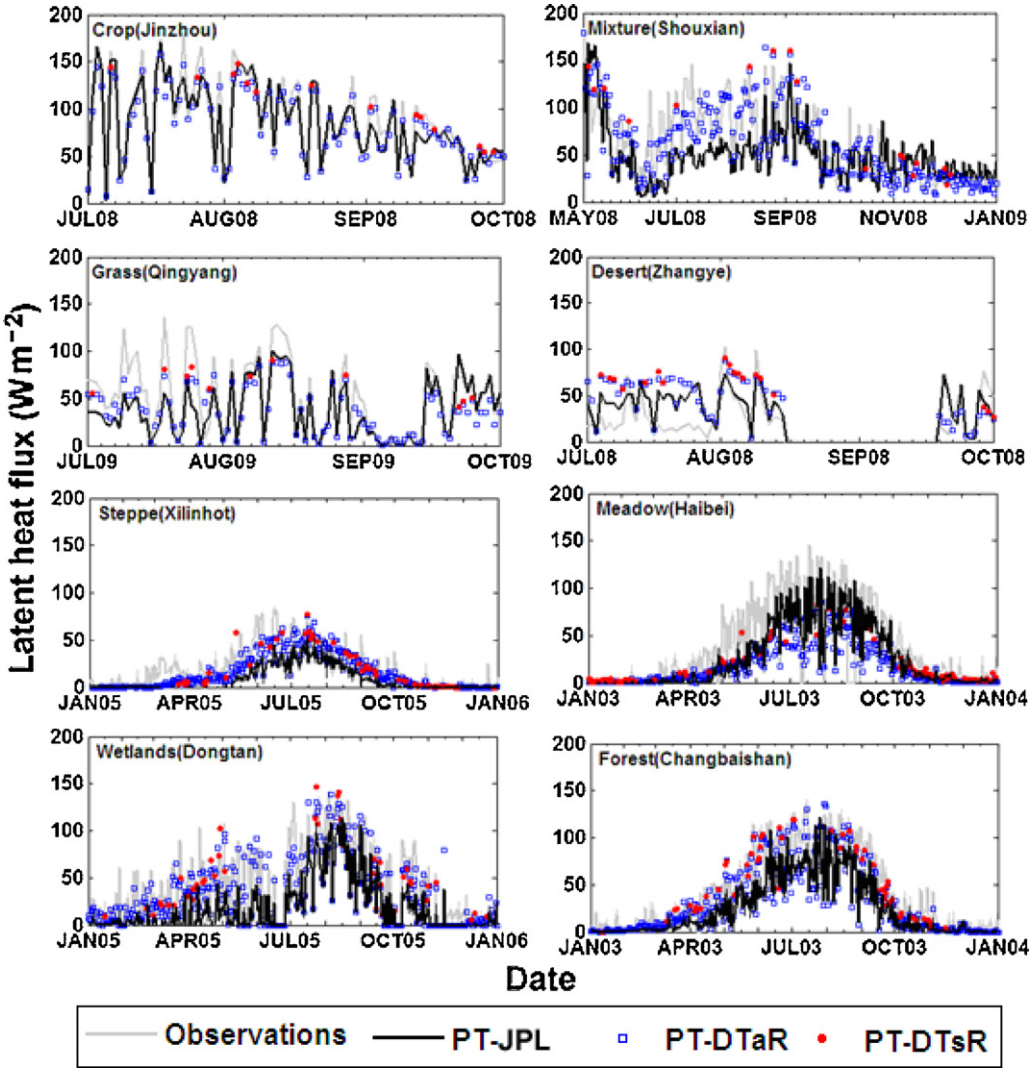

Fig. 6. Time series comparisons of the modeled latent heat flux (daily total) estimates based on three *PT* algorithms and the ground-measured latent heat flux using the data collected from the 8 flux towers in their respective land cover classes from the validation tower set. All *r* values are significant with 99% confidence.

Table 3
Statistics of estimated daily surface latent heat flux against the eddy-flux tower observations.

Tower	Bias (W m^{-2})			*RMSE* (W m^{-2})			R^2		
	PT-DTsR	*PT-DTaR*	*PT-JPL*	*PT-DTsR*	*PT-DTaR*	*PT-JPL*	*PT-DTsR*	*PT-DTaR*	*PT-JPL*
Dongsu	−6.9	−3.4	−20.8	14.7	14.2	21.6	0.60	0.35	0.31
Jinzhou	−8.9	−5.3	−11.4	16.2	12.7	21.1	0.97	0.96	0.79
Miyun	−13.5	−9.8	−17.1	15.4	11.6	21.5	0.96	0.96	0.87
Shouxian	3.7	5.6	6.6	16.8	17.6	20.9	0.90	0.90	0.77
Tongyu	11.7	12.3	11.7	14.3	15.2	14.9	0.95	0.93	0.91
Guantao	−11.5	−6.9	−21.8	12.9	8.4	25.8	0.96	0.95	0.78
Qingyang	−27.6	−29.5	−35.4	30.5	33.4	39.7	0.81	0.71	0.53
Shapotou	−6.8	−7.6	−24.2	9.7	10.9	26.7	0.41	0.45	0.31
Laoshan	4.5	3.9	−2.1	4.8	5.9	3.8	0.83	0.31	0.53
Dinghushan	−3.8	−2.2	−6.1	9.9	11.3	16.9	0.97	0.96	0.90
Yueyang	−17.9	−16.9	−23.8	21.3	19.8	30.4	0.96	0.95	0.89
Xilinhot	0.2	1.7	−8.1	12.6	13.4	14.6	0.70	0.69	0.68
Changbaishan	−8.6	−6.7	−19.8	13.8	12.9	22.5	0.91	0.91	0.89
Dongtan	−12.1	−13.2	−27.1	19.8	18.9	31.7	0.80	0.80	0.74
Haibei	−14.4	−17.7	−14.1	24.8	26.7	20.2	0.93	0.92	0.89
Zhangye	6.6	5.9	5.2	24.4	24.2	23.3	0.22	0.22	0.16
Average	−6.6	−5.6	−13.1	17.8	18.4	22.3	0.87	0.86	0.83

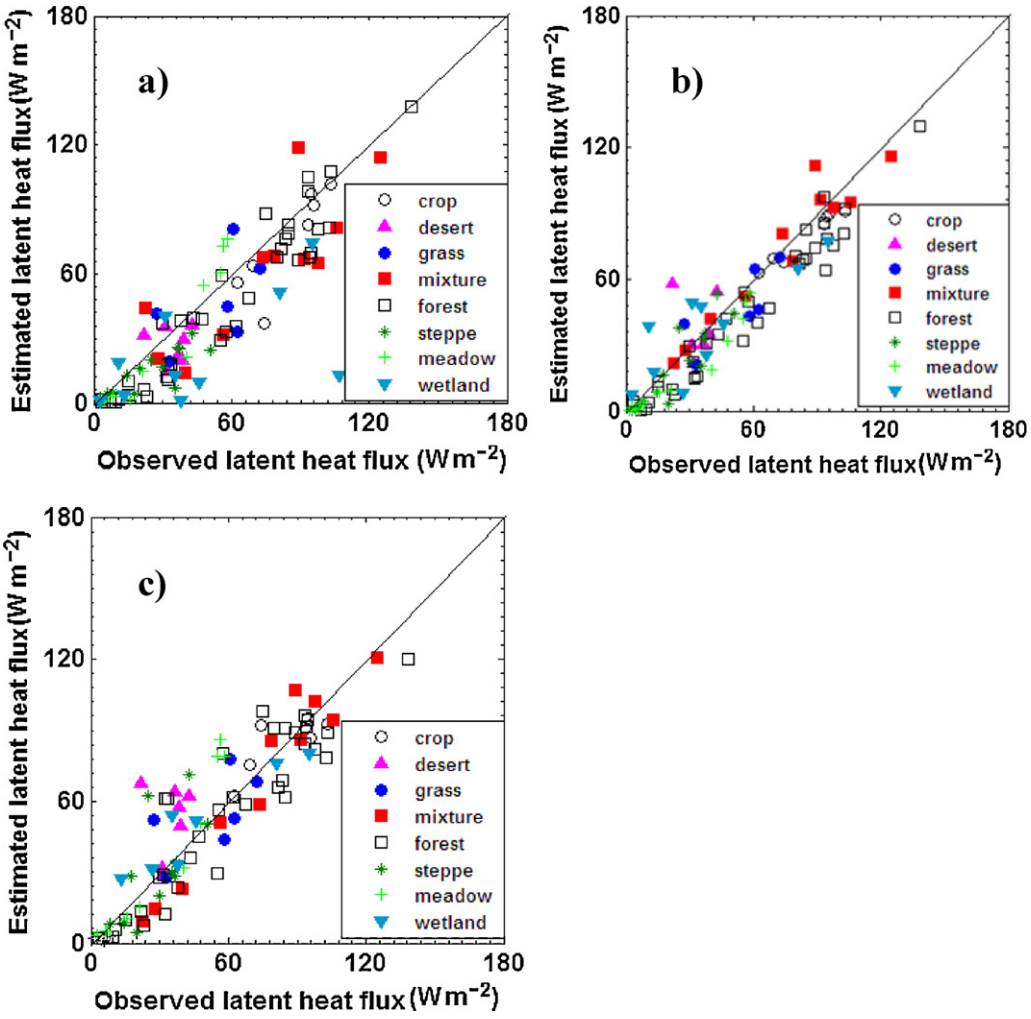

Fig. 7. (a) Independent validation of the monthly estimated *LE* based on the *PT-JPL LE* algorithm derived from 16 flux towers at different biome types shown in Table 2. (b) Independent validation of the monthly estimated *LE* based on the *PT-DTaR* model using the data from 16 flux towers at different biome types shown in Table 2. (c) Independent validation of the monthly estimated *LE* from *MODIS* products at 0.05° and the observed *LE* at 16 flux towers at different biome types shown in Table 2. These relationships are significant with 99% confidence.

The confidence levels of the derived tendencies are calculated according to the Student's *t*-test distribution with $n-2$ degrees of freedom (Pinker et al., 2005).

$$t = r_{xy}\sqrt{\frac{n-2}{1-r_{xy}^2}} \tag{20}$$

Here, r_{xy} is the correlation coefficient between the original time series and the linear-fitted time series, and n is the number of observations. We have applied the linear trend analysis pixel-wise to calculate the *LE* trend for each pixel. We also calculated the regional average time series and then applied the linear trend analysis to quantify the regional *LE* trends.

3. Results and discussion

3.1. Regional air temperature and net radiation estimation

3.1.1. Implementation of regional air temperature algorithm

We have implemented the air temperature estimation algorithm in China to further demonstrate its reliability. We have selected T_a, *NDVI*, LST_{day}, and LST_{night}, as the input parameters for linear regression to yield Eq. (9) for air temperature estimation based on monthly meteorological data, monthly *MODIS-NDVI* composite products and *MODIS-LST* composite products with a 0.05° spatial resolution covering 2001–2005 from 752 meteorological stations across continental China (Fig. 3). Considering that these meteorological stations cover all the provinces of China, we find these sufficiently representative for the purpose of estimating T_a (°C) in China using T_s (°C) and *NDVI*.

$$T_a = -2.911 + 0.910T_s + 7.606NDVI \tag{21}$$

Fig. 4a shows scatter plots of a comparison between the monthly estimated and observed air temperature using near surface observation data, *MODIS LST* products and *MODIS NDVI* products. We observe that the bias of the estimated air temperature for all 752 meteorological stations is −0.05 °C. The *RMSE* is 2.24 °C, and the R^2 is approximately 0.96. The accuracy of the monthly near surface air temperature simulation can be used to estimate the surface net radiation and latent heat flux in China.

To fairly evaluate the accuracy of the near surface air temperature estimation in China, the monthly near surface air temperature, estimated based on Eq. (21) from *MODIS* data with 1 km spatial resolution, has been independently validated using the observed data collected from 16 flux towers. The estimated air temperature is correlated with the tower measurements, with an R^2 of approximately 0.96, an *RMSE* of approximately 2.45 °C, and a low bias of approximately 0.56 °C (Fig. 4b). The resulting *RMSE* of 2.45 °C is relatively low, considering the estimated error of the input *LST* (the accuracy

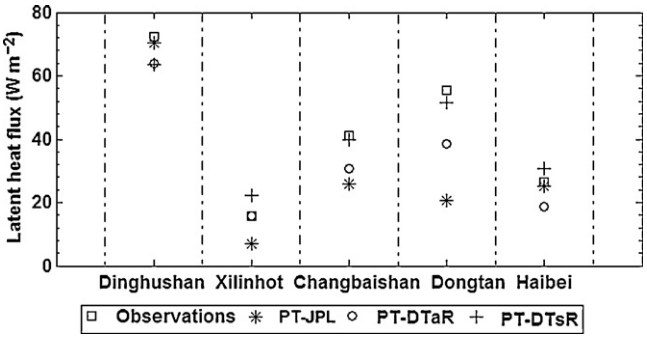

Fig. 8. Comparisons of modeled and measured annual latent heat flux at the 5 representative validation tower sites.

of the input *LST* is slightly better than 2 °C). The spatial distribution of the average near surface air temperature for 2001 in China is plotted in Fig. 4c, which shows the strong regional variations corresponding to the climate patterns. The sub-tropical forest regions show the highest annual air temperature, while Qinghai-Tibet and the Northeast areas within the cold-temperate regions show the lowest annual air temperature.

3.1.2. Estimation and validation of regional net radiation

Monthly net radiation estimates at a 0.05° spatial resolution are constructed using *MODIS* Insolation, *MODIS* albedo for shortwave radiation, *MODIS* land surface temperature and emissivity for longwave upward radiation and the near surface air temperature

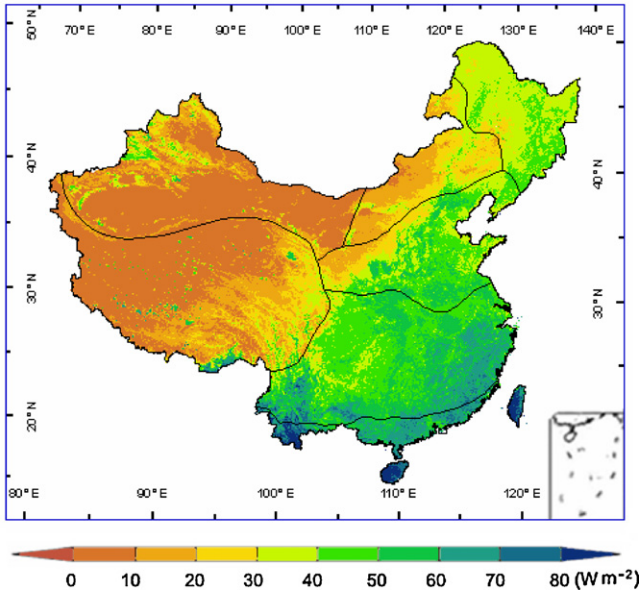

Fig. 9. Map of multiyear (2001–2010) mean annual *LE* in China as derived from the modified satellite-based Priestley–Taylor *ET* model using R_n, *NDVI*, T_a, and *DTsR* from *MODIS* products.

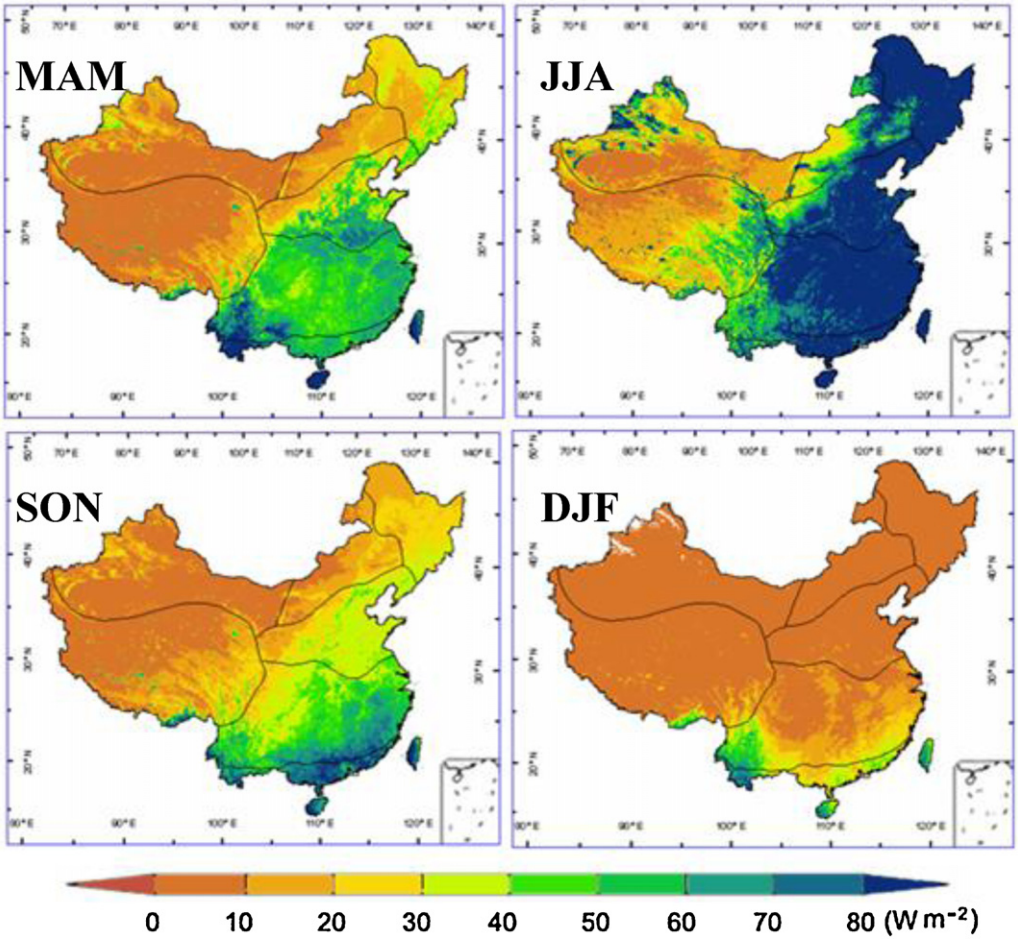

Fig. 10. Multiyear (2001–2010) mean seasonality of *LE* in China.

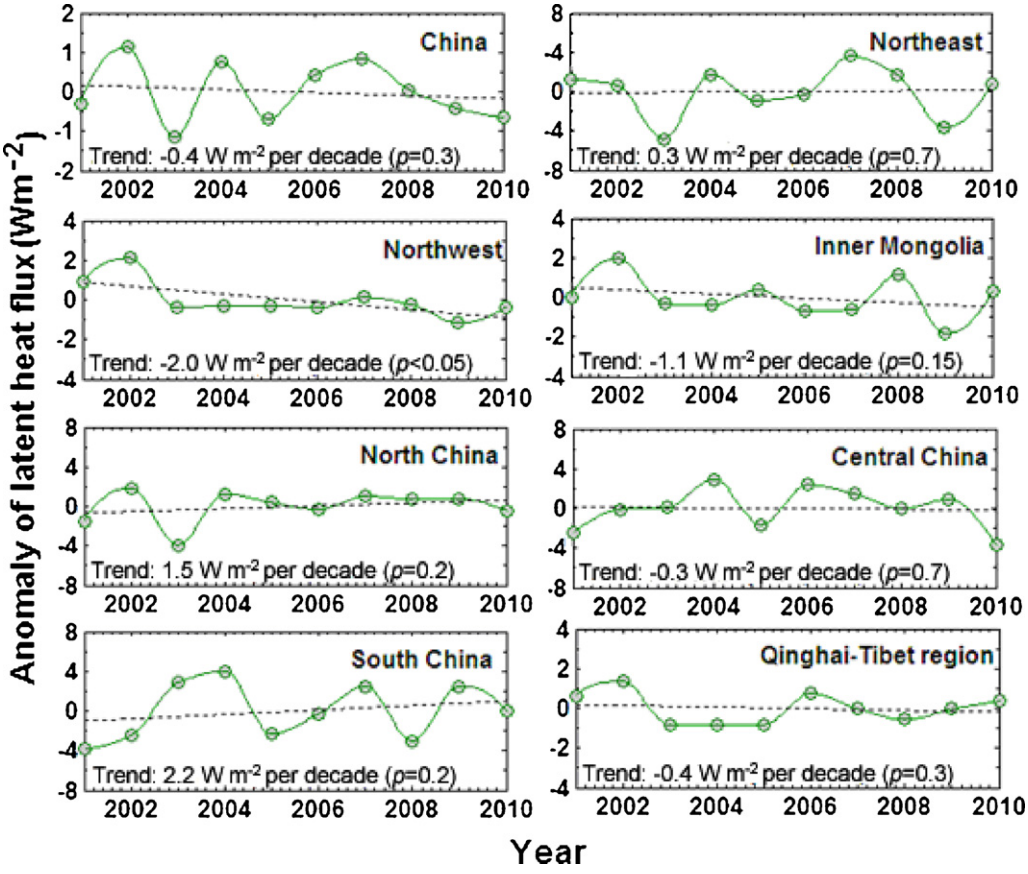

Fig. 11. Regional and terrestrial averaged annual *LE* anomalies in China. Dashed lines represent the linear trends in the *LE* estimated using the *MODIS* products (unit: W m^{-2} per decade).

derived from Eq. (21) for longwave downward radiation. Although rigorous validation of the surface radiation flux derived from the remote sensing data described here presents a challenging problem due to the deficiency of the time-continuous flux measurements at a scale of at least 0.05°, the tower measurements may sample the variability of the radiation flux in the heterogeneous landscape at a 0.05° scale. Therefore, we have selected 16 flux towers shown in Table 2 to validate the estimated surface net radiation. Over all the sites, the estimated monthly net radiation from *MODIS* agreed well with the tower measurements, with a correlation coefficient of 0.88 ($p < 0.01$), *RMSE* of 23.9 W m^{-2}, and bias of 8.5 W m^{-2} (Fig. 5a). The positive bias may result from (1) the accumulated error of inputs of the *MODIS* products, including *albedo*, *LST* and *Insolation*, (2) the differences of scaling from tower footprints to satellite mixed pixels, and (3) the accuracy of the surface net radiation algorithm simulation. As shown in Fig. 5b, the spatial distribution of net radiation for 2001 in China shows that the largest fluxes occur in the Qinghai-Tibet areas, followed by the dry regions (e.g., Northwest and North China) and the humid temperate regions in Northeast China and Inner Mongolia. Small net radiation fluxes occur in subtropical environments due to the higher cloud cover fraction.

3.2. Validation of latent heat flux estimates

3.2.1. Model validation

Our modeled *LE* has been compared against the *LE* measured by the eddy covariance method (Baldocchi et al., 2001) at the towers for the respective range of footprints. The time series comparisons of the modeled *LE* (daily total) estimates based on three *PT* methods and ground-measured *LE* using the data collected from the 8 flux towers are plotted in Fig. 6. In general, the modeled and measured seasonal curves show good agreement, although the model *LE* based on our modified *LE* model tends to underestimate the tower observations for meadow sites. This *LE* underestimation is likely due to wet soil and low vegetation cover in the meadow sites, resulting in a greatly reduced vegetation transpiration controlling factor and enhanced evaporation. For all 16 validation sites, the *LE* simulations using our modified *LE* model show generally better results than the *PT-JPL* method (Table 3). For both the *PT-DTsR* and the *PT-DTaR* model, the average daily bias for all sites is −6.6 W m^{-2} and −5.6 W m^{-2}, respectively, the average *RMSE* is 17.8 W m^{-2} and 18.4 W m^{-2}, respectively, and the average R^2 is 0.87 and 0.86, respectively. However, the overall R^2 for the comparison between the measured and modeled daily *LE* using the *PT-JPL* model is 0.83, the *RMSE* is 22.3 W m^{-2} and the bias is −13.1 W m^{-2} (Table 3). The negative bias may partly be from the energy imbalance issue encountered in the eddy covariance method. The standard deviations and correlation coefficients at the flux towers are very good (Table 3) at the different land cover types, indicating that the modified *PT* method proposed in this study works well.

On a monthly basis, the model *LE* results using both *PT-DTaR* and *PT-JPL* derived from tower-measured data agree well with the *LE* observations from all 16 tower sites (Fig. 7). The tower-driven results using the *PT-DTaR* model account for 91% of the observed variation in the monthly *LE* measurements, with respective *RMSE* and bias differences of 12.5 W m^{-2} and −6.4 W m^{-2}, while the tower-driven results using the *PT-JPL* model explain only 78% of the variation in the measured *LE*, with respective *RMSE* and bias values of 19.4 W m^{-2} and −10.3 W m^{-2}. Similarly, the monthly estimated results based on *PT-DTsR* from the *MODIS* products at 0.05° spatial resolution are also compared with the ground observations

corresponding to the specific land-surface type associated with the site, and they account for approximately 83% of the observed variation in monthly *LE* measurements. This finding may be attributed to the fact that the local tower conditions were poorly represented by the coarse *MODIS* products at several sites, reducing the overall performance of the *MODIS*-driven results. Despite this sub-pixel heterogeneity, it is essential to observe that the inputs for *PT-DTsR* consist of uniform values for the entire grid box (Miralles et al., 2011). Importantly, the *MODIS*-driven results show similar performance to the tower-driven results at most flux towers.

To identify the annual bias for variations of multiyear *LE*, the *LE* annual anomaly validation can be considered a good choice (Wang et al., 2010a). However, with only 5 flux towers covering one year of reliable data, we have compared the modeled and measured annual latent heat flux at the 5 validation tower sites, including forest, grass, meadow and wetland (Fig. 8). The results illustrate that the *PT-DTsR* model offers the highest simulation accuracy for annual *LE* at the 5 flux towers, with an R^2 of 0.96, *RMSE* of 5.8 W m^{-2} and bias of −1.2 W m^{-2}, followed by the *PT-DTaR* model and the *PT-JPL* model. Although radiation forcing and uncertainty across models exists in different *LE* algorithms, considering that our modified *LE* model results show small biases for algorithm validation, the high coefficients of determination (R^2), low *RMSE*, and bias for monthly and annual *LE* results indicate that the satellite-based algorithm generally captures the observed seasonal and inter-annual variations and the site-to-site differences in *LE* (Zhang et al., 2010; Jung et al., 2010).

3.2.2. Algorithm advantages and limitations

Advantages offered by the modified Priestley–Taylor *LE* model over other complicated physical *ET* models are that (1) the modified model is easy to operate for routine, long-term mapping of *LE* because it only needs four inputs, namely, net radiation, *NDVI*, air temperature and diurnal temperature range; and (2) the *LE* algorithm used by the modified model avoids the computational complexities of aerodynamic resistance parameters.

Accurate estimation of terrestrial *LE* is a challenging scientific problem because soil surface evaporation and plant transpiration processes involve a large number of physical factors, such as micro-meteorology, plant biophysics for site-specific species and landscape heterogeneity (Friedl, 1996; McVicar et al., 2007; Mu et al., 2007, 2011). The following limitations remaining in our modified *PT* model can effectively account for the differences between the observed *LE* from flux towers and the modeled *LE:* (1) Our modified *PT* algorithm has been developed by revising the expression of different controlling *LE* factors (energy, water and temperature constraints) for all climatic zones without considering the differences of parameters in different biome types. However, for different biome types within the same climatic zones, differences in these parameters may exist (Nemani et al., 2003; Turner et al., 2003; Mu et al., 2011). Thus, there may be small biases between the observed and the modeled *LE*. (2) The effects of CO_2 on *LE* are not included in our model. Despite the fact that increases in leaf area index (*LAI*) or *NDVI* can largely compensate for the decreases in plant transpiration due to high-CO_2-induced partial stomatal closure, the daily total *LE* may be underestimated (Idso and Brazel, 1984; Piao et al., 2007; Wang et al., 2010a,b; Yao et al., 2012). For one decade, this effect on *LE* may be negligible, but for additional decades, this effect should be considered (Zhang et al., 2009; Mu et al., 2011). (3) The mechanisms of soil heat fluxes and soil boundary layer resistance are still uncertain. We have estimated soil heat fluxes using a simple semi-empirical method in this paper. As a result, we may overestimate soil heat fluxes and underestimate the *LE*. Therefore, a satellite-based method for estimating soil heat fluxes in different ecosystems needs to be explored in the future.

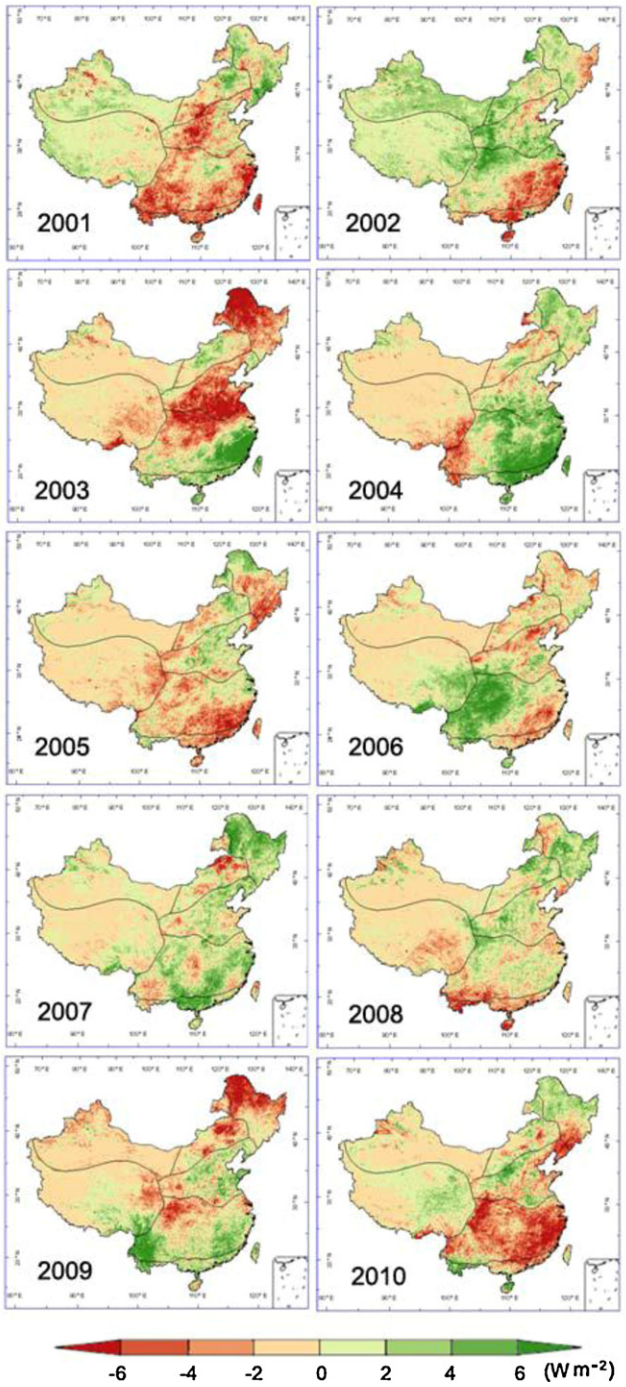

Fig. 12. Spatial representation of *LE* derived from the *MODIS* products anomaly for ten years, 2001–2010. "Anomaly" refers to the annual value for each year minus the 10-year average.

3.3. China's latent heat flux patterns

We have applied *PT-DTsR* with the monthly *MODIS* products (*Insolation*, *albedo*, *LST*, *NDVI*, etc.) inputs to estimate the monthly *LE* in China at a 0.05° spatial resolution from 2001 through 2010. The multiyear (2001–2010) average annual *LE* is plotted in Fig. 9, which shows strong regional variations and latitudinal gradients corresponding to climate patterns in China (Zhang et al., 2010). The largest *LE* occurs in the tropical and subtropical regions (South and Central China), followed by the temperate and boreal forest regions in North and Northeast China. A small *LE* flux occurs

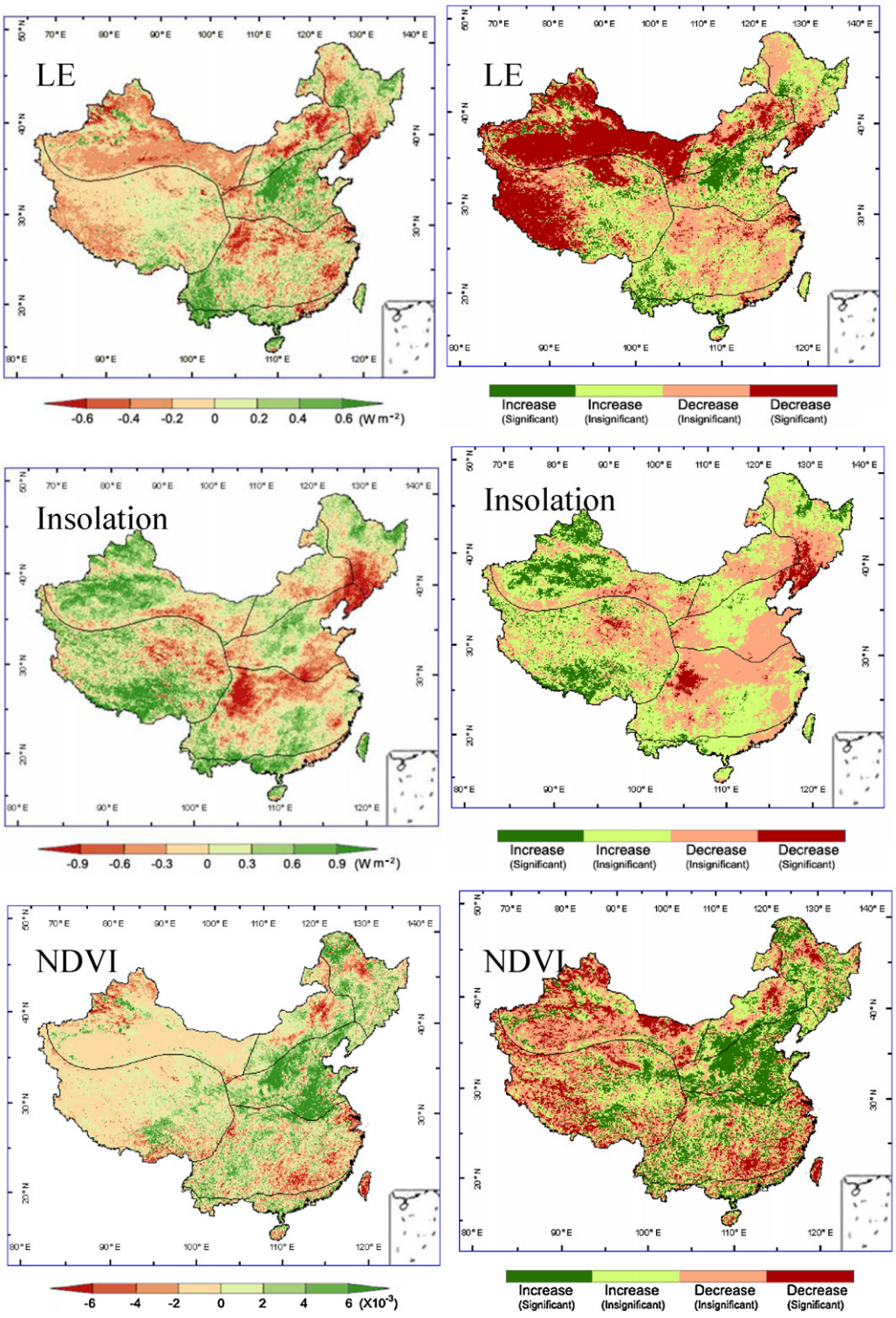

Fig. 13. Maps of the linear trend in estimated *LE*, Insolation from *JAXA*, and *MODIS-NDVI* from 2001 through 2010. The trends are classified into four categories according to statistical linear trend analysis: significant increase ($p < 0.1$), significant decrease ($p < 0.1$), insignificant increase ($p > 0.1$) and insignificant decrease ($p > 0.1$).

in the dry and lower temperature regions including Northwest China, Inner Mongolia and the Qinghai-Tibet region of China. The terrestrial average annual *LE* in China is $28.7 \pm 1.1\,W\,m^{-2}$, equal to 364.9 ± 14.6 mm. The Evergreen Broadleaf Forest biome has the highest average *LE* of $68.3 \pm 3.7\,W\,m^{-2}$, followed by Permanent Wetland ($56.2 \pm 4.6\,W\,m^{-2}$), Mixed Forest ($47.3 \pm 2.8\,W\,m^{-2}$), Deciduous Broadleaf Forest ($43.7 \pm 2.8\,W\,m^{-2}$), Crop Land ($40.9 \pm 3.1\,W\,m^{-2}$), Evergreen Needleleaf Forest ($34.5 \pm 2.4\,W\,m^{-2}$), Closed Shrubland ($33.8 \pm 1.9\,W\,m^{-2}$), Deciduous Needleleaf Forest ($34.4 \pm 5.8\,W\,m^{-2}$), Grassland ($20.2 \pm 1.7\,W\,m^{-2}$), Open Shrubland ($12.6 \pm 1.2\,W\,m^{-2}$) and Barren Lands ($7.5 \pm 1.6\,W\,m^{-2}$). Although some uncertainties are present, the *LE* magnitudes and spatial pattern of *LE* in China is generally consistent with previous reports (Mu et al., 2007; Jung

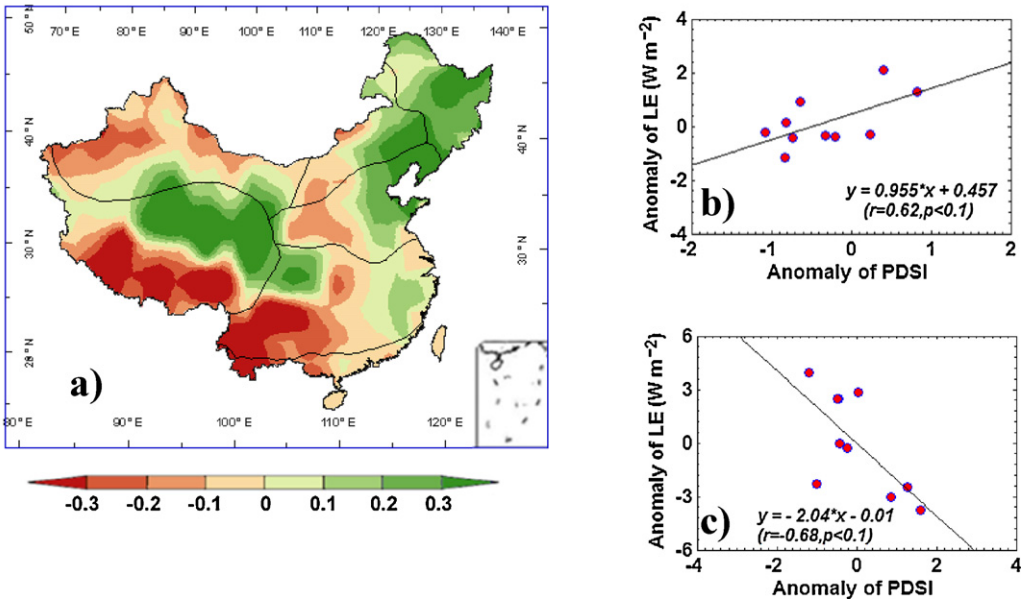

Fig. 14. (a) Map of the linear trend in *PDSI* in China during 2001–2010; (b) the scatter plot between the anomaly of *LE* and the *PDSI* over Northwest China; and (c) the scatter plot between the anomaly of *LE* and the *PDSI* over South China.

et al., 2010; Zhao and Running, 2010). Gao et al. (2007) used the modified water balance methodology and found that the annual actual *ET* varied from 20 mm in the northwest to 1000 mm in the southeast of China. Zhang et al. (2010) used 1983–2006 satellite records to calculate the annual *ET* and reported an annual *ET* of 635 ± 200 mm, 507 ± 157 mm, 311 ± 193 mm and 352 ± 166 mm for Deciduous Broadleaf Forest, Cropland, Grassland and Closed Shrubland, respectively.

The multiyear mean seasonal patterns of *LE* in China from 2001 through 2010 based on the *PT-DTsR* model with monthly *MODIS* product inputs shows obvious global seasonality (Fig. 10). We find that the sub-tropical and temperate regions in North and Central China exhibit higher seasonal variability than the tropics, while the tropical regions of South China still show high *LE* values throughout the different seasons. These spatial distribution maps supply an important background and physical interpretation for energy, water and climate change in China.

3.4. Variations of terrestrial latent heat flux in China

On the whole, the estimated terrestrial *LE* in China after removal of the mean annual cycle shows a trend toward a small decrease on average for the 2001–2010 period (-0.4 W m^{-2} per decade; $p = 0.3$), coinciding with widespread regional drought and net radiation decline (Qi et al., 2011; Qian et al., 2011) (Fig. 11). Especially in 2001, 2003, 2005 and 2010, the *LE* values were significantly lower than the annual mean values in China because severe drought occurred during these periods (Qian et al., 2011) (Fig. 12). Fig. 13 shows the spatial pattern of *LE* trends from 2001 through 2010. The *LE* decreased over large areas in Central China, Northwest China and Inner Mongolia while increasing in the Northeast, North and South regions of China. The *LE* results show generally negative trends for 61% of the entire China domain (Fig. 13). Approximately 54% of the areas showing significant negative *LE* trends occur in the Northwest and Inner Mongolia regions of China, while the forest and croplands of North China show significant positive *LE* trends.

Regionally, the *LE* in Central China, Northwest China and Inner Mongolia explains 60% of the variations in the terrestrial *LE* of China. In these areas, the negative annual *LE* is mainly caused by large-scale droughts (Lu et al., 2011; Barriopedro et al., 2012). However, in Central China, in addition to drought, substantial increases of aerosol optical depth (*AOD*) caused by industrial activity have decreased the *LE* by reducing solar radiation on the Earth's surface by upward reflection and absorption (Zhou et al., 2004; Wang et al., 2009; Zheng et al., 2011). As shown in Fig. 13, the spatial variation of the *LE* and the solar radiation anomalies show the same general trends, and the spatial correspondences support the lack of sunlight as the cause of the change in *LE* (Myneni et al., 2007; Sasai et al., 2011). As a result, in 2003, because the annual mean solar radiation is relatively low, plant photosynthesis activity and *LE* have dropped across China.

For vegetated land areas of Northeast, North and South China, large scale afforestation and agricultural intensification, such as the Three-Norths Shelter Forest System Project and South Natural Forest Protection Project, have increased *NDVI* and the vegetation cover, thus increasing the terrestrial *LE* (Cao, 2008) (Fig. 13). Although the tropical forest regions of South China have experienced drying trends during recent years (especially an intense drought episode in 2010), the *LE* shows a positive trend (2.2 W m^{-2} per decade, $p = 0.17$). Besides human activities, this finding may also partially be attributed to the fact that solar radiation plays a dominant role in controlling vegetation growth, and the *LE* in the humid tropical regions, in which forests rarely experience soil moisture limitations due to an ample supply of moisture, as well as to the fact that fewer clouds during drought permit more sunlight to reach the surface and the vegetation activity may be higher in the dry season than in the wet season (Nepstad et al., 1994; Schenk and Jackson, 2005; Huete et al., 2006; Myneni et al., 2007; Teuling et al., 2009; Seneviratne et al., 2010; Wang and Dickinson, 2012). Thus, a significant positive correlation ($r = 0.62$, $p < 0.1$) was found between the anomaly of *LE* and the *PDSI* in the arid and semi-arid regions of Northwest China, while only a significant negative correlation ($r = -0.68$, $p < 0.1$) was found in the humid tropical regions of South China (Fig. 14). For the Qinghai-Tibet plateau with an average elevation of more than 4000 m, increasing *LE* occurs in the east while *LE* tends to decrease in western Qinghai-Tibet regions. These may be due to the increasing precipitation in eastern areas and the decline of precipitation in the west of the domain associated with climate warming during the recent 10-year period (Wang et al., 2012).

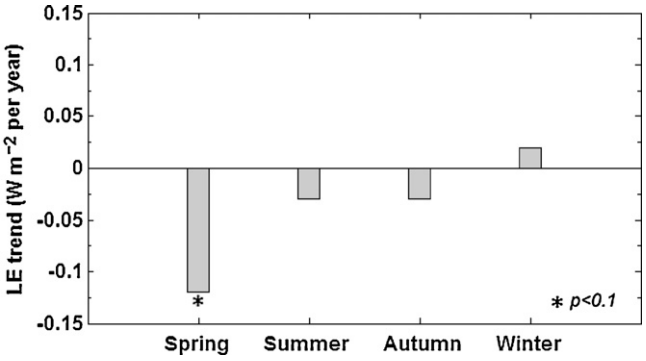

Fig. 15. Seasonal trends of average *LE* in China derived from *MODIS* products between 2001 and 2010.

A seasonal change of the terrestrial *LE* in China during the 10-year period is most noticeable (Fig. 15). The *MODIS*-derived *LE* shows negative trends in spring, summer and autumn, with a slightly increasing trend in winter. The largest significant decline of the *LE* occurs in the spring followed by summer and autumn. These results suggest that large-scale severe drought episodes offset the positive *LE* effects of afforestation and contribute to the decreases in seasonal *LE*, while the positive *LE* trend in winter is associated with the lengthening of the seasonal non-frozen period caused by global warming (Zhang et al., 2009; Yang et al., 2012). For the growing season, the larger negative *LE* trends in spring, summer and autumn indicate that China became dryer during the past decade. In contrast, the slightly positive *LE* trends illustrate that China became wetter during the winter periods of 2001–2010.

4. Summary and conclusion

Latent heat flux remains one of the greatest unknowns within the global energy, water and carbon cycles. To better understand the spatio-temporal dynamics of *LE* in China, we have modified the satellite-based Priestley–Taylor *LE* model, based on the *PT-JPL* model, to estimate China's latent heat flux on a month's time scale. This algorithm quantifies the Priestley–Taylor coefficient to estimate the *LE* over a wide range of climate conditions using the satellite-derived *NDVI*, net radiation, air temperature and diurnal temperature range. Meanwhile, a semi-empirical air temperature algorithm based on *MODIS* observations and meteorological observations has been designed to estimate China's monthly air temperature at a 0.05° spatial resolution.

Overall, the estimated seasonal *LE* using the new model agreed well with the tower measurements. The daily *RMSE* is reduced from 22.3 W m^{-2} from the *PT-JPL LE* model to 17.8 W m^{-2} with our modified approach (*PT-DTsR*). The R^2 increased from 0.83 to 0.87, averaged over all sites for validation, and the mean biases are also reduced accordingly. Our satellite-based *LE* algorithm generally captures the observed seasonal and inter-annual variations and site-to-site differences in the *LE*.

The spatial distribution of our modeled mean annual *LE* at 0.05° spatial resolution has followed the patterns of *NDVI* distribution and the *LE* magnitudes and the spatial pattern of the *LE* in China is generally consistent with the findings of other studies. Importantly, the spatial variation of the annual *LE* anomaly in China is completely different in different climatic zones: the *LE* has decreased over large areas in Central China, Northwest China and Inner Mongolia, while increasing in the Northeast, North and South regions of China. A large-scale drought and the afforestation may account for the variations in the terrestrial *LE* in China. An important next step is to extend our analysis to quantify how the human-induced land-use change affects the latent heat flux and the sensible heat flux exchange in various ecosystems.

Acknowledgements

The authors thank the anonymous reviewers for their critical and helpful comments and suggestions. The authors would like to thank Dr. Xianhong Xie, Dr. Wenping Yuan, Dr. Xianglan Li, Dr. Xiaotong Zhang, Dr. Bo Jiang and Dr. Liang Sun from the College of Global Change and Earth System Science, Beijing Normal University, China, for their suggestions. The authors would like to thank Dr. Qibing Wang from the State Key Labratory of Vegetation and Environmental Change, Institute of Botany, Chinese Academy of Sciences, for his help. The authors would also like to extend their thanks to China Meteorological Administration (*CMA*) for providing ground-measured meteorological data. Latent heat flux, net radiation, shortwave solar radiation and corresponding meteorological observations were obtained from the Coordinated Enhanced Observation Project (*CEOP*) in arid and semi-arid regions of northern China (http://observation.tea.ac.cn/), the water experiments of Environmental and Ecological Science Data Center for West China (http://westdc.westgis.ac.cn/water), the Atmosphere Radiation Measurement (*ARM*) Program of the U.S. Department of Energy (http://www.archive.arm.gov/), the *ChinaFlux* network (http://www.chinaflux.org/index/index.asp), the Japan Aerospace Exploration Agency (*JAXA*) (http://suzaku.eorc.jaxa.jp/GLI/data/final/landpar/index.html). *DEM* data was derived from Shuttle Radar Topography Mission (*STRM*) *DEM* data (http://datamirror.csdb.cn/dem/search.jsp). The monthly *PDSI* products were derived from the NCAR CGD's Climate Analysis Section dataset (http://www.cgd.ucar.edu/cas/catalog/climind/pdsi.html). *MODIS NDVI*, *LST*, *albedo* and land cover satellite products were obtained online (http://reverb.echo.nasa.gov/reverb). This work was partially supported by the Special Foundation for Free Exploration of State Laboratory of Remote Sensing Science (Grant No. ZY12-11), the Natural Science Fund of China (No. 41201331, No. 40901167 and No. 41101313), the High-Tech Research and Development Program of China (No. 2009AA122100), the Advance Research Program of Civil Aerospace Technology: Research on the Key Techniques in Remote Sensing Data Processing for Solid Surface Elements Extraction. J.B.F. contributed to this paper from the Jet Propulsion Laboratory, California Institute of Technology, under a contract with the National Aeronautics and Space Administration.

References

Anderson, M.C., Norman, J.M., Diak, G.R., Kustas, W.P., Mecikalski, J.R., 1997. A two-source time-integrated model for estimating surface fluxes using thermal infrared remote sensing. Rem. Sens. Environ. 60, 195–216.

Anderson, M.C., Norman, J.M., Mecikalski, J.R., Otkin, J.A., Kustas, W.P., 2007. A climatological study of evapotranspiration and moisture stress across the continental United States based on thermal remote sensing: 1. Model formulation. J. Geophys. Res. 112, D10117.

Baldocchi, D., Falge, E., Gu, L.H., Olson, R., Hollinger, D.Y., Running, S.W., Anthoni, P., Bernhofer, C.H., Davis, K.J., Evans, R., Fuentes, J., Goldstein, A., Katul, G., Law, B.E., Lee, X., Malhi, Y., Meyers, T.P., Munger, J.W., Oechel, W.C., Paw, K.T., Pilegaard, U.K., Schmid, H.P., Valentini, R., Verma, S., Vesala, T., Wilson, K.B., Wofsy, S.C., 2001. FLUXNET: a new tool to study the temporal and spatial variability of ecosystem-scale carbon dioxide, water vapor and energy flux densities. Bull. Am. Meteorol. Soc. 82, 2415–2434.

Barriopedro, D., Gouveia, C.M., Trigo, R.M., Wang, L., 2012. The 2009/10 drought in China: possible causes and impacts on vegetation. J. Hydrometeorol. 13, 1251–1267.

Bastiaanssen, W.G.M., Menenti, M., Feddes, R.A., Holtslag, A.A.M., 1998. A remote sensing surface energy balance algorithm for land (SEBAL). 1. Formulation. J. Hydrol. 213, 198–212.

Bouchet, R.J., 1963. Evapotranspiration reelle evapotranspiration potentielle, signification climatique. Int. Assoc. Sci. Hydrol., 134–142.

Cao, S.X., 2008. Why large-scale afforestation efforts in China have failed to solve the desertification problem. Environ. Sci. Technol. 42, 1826–1831.

Cleugh, H.A., Leuning, R., Mu, Q., Running, S.W., 2007. Regional evaporation estimates from flux tower and MODIS satellite data. Rem. Sens. Environ. 106, 285–304.
Fisher, J.B., Tu, K.P., Baldocchi, D.D., 2008. Global estimates of the land atmosphere water flux based on monthly AVHRR and ISLSCP-II data, validated at 16 FLUXNET sites. Rem. Sens. Environ. 112, 901–919.
Friedl, M.A., 1996. Relationships among remotely sensed data, surface energy balance, and area-averaged fluxes over partially vegetated land surfaces. J. Appl. Meteorol. 35, 2091–2103.
Gao, G., Chen, D.L., Xu, C.Y., Simelton, E., 2007. Trend of estimated actual evapotranspiration over China during 1960–2002. J. Geophys. Res. 112, D11120.
Gash, J.H.C., 1987. An analytical framework for extrapolating evaporation measurements by remote sensing surface temperature. Int. J. Remote Sens. 8, 1245–1249.
Halliwell, D.H., Rouse, W.R., 1987. Soil heat flux in permafrost: characteristics and accuracy of measurement. J. Climate 7, 571–584.
Huete, A.R., Didan, K., Shimabukuro, Y.E., Ratana, P., Saleska, S.R., Hutyra, L.R., Yang, W.Z., Nemani, R.R., Myneni, R., 2006. Amazon rainforests green-up with sunlight in dry season. Geophys. Res. Lett. 33, L06405.
Idso, S.B., Jackson, R.D., 1969. Thermal radiation from the atmosphere. J. Geophys. Res. 74, 5397–5403.
Idso, S.B., Brazel, A.J., 1984. Rising atmospheric carbon dioxide concentrations may increase stream flow. Nature 312, 51–53.
Jackson, R.D., Reginato, R.J., Idso, S.B., 1977. Wheat canopy temperature: a practical tool for evaluating water requirements. Water Resour. Res. 13, 651–656.
Jacobs, J.D., 1978. Radiation Climate of Broughton Island, Energy Budget Studies in Relation to Fast-ice Breakup Processes in Davis Strait, vol. 26. Occas Pap. Inst. of Arctic and Alp Res, University of Colorado, United States, pp. 105–120.
Jiang, L., Islam, S., 2001. Estimation of surface evaporation map over southern Great Plains using remote sensing data. Water Resour. Res. 37, 329–340.
Jin, Y.F., Randerson, J.T., Goulden, M.L., 2011. Continental-scale net radiation and evapotranspiration estimated using MODIS satellite observations. Rem. Sens. Environ. 115, 2302–2319.
Jung, M., Reichstein, M., Ciais, P., Seneviratne, S.I., Sheffield, J., Goulden, M.L., Bonan, G., Cescatti, A., Chen, J., de Jeu, R., Dolman, A.J., Eugster, W., Gerten, D., Gianelle, D., Gobron, N., Heinke, J., Kimball, J., Law, B.E., Montagnani, L., Mu, Q.Z., Mueller, B., Oleson, K., Papale, D., Richardson, A.D., Roupsard, O., Running, S., Tomelleri, E., Viovy, N., Weber, U., Williams, C., Wood, E., Zaehle, S., Zhang, K., 2010. Recent decline in the global land evapotranspiration trend due to limited moisture supply. Nature 467, 951–954.
Kustas, W.P., Norman, J.M., 1996. Use of remote sensing for evapotranspiration monitoring over land surfaces. Hydrol. Sci. J. 41, 495–516.
Liang, S.L., Wang, K.C., Zhang, X.T., Wild, M., 2010. Review of estimation of land surface radiation and energy budgets from ground measurements, remote sensing and model simulation. IEEE J. STARS 3, 225–240.
Lu, E., Luo, Y.L., Zhang, R.H., Wu, Q.X., Liu, L.P., 2011. Regional atmospheric anomalies responsible for the 2009–2010 severe drought in China. J. Geophys. Res. 116, D21114.
L'vovich, M.I., White, G.F., 1990. Use and transformation of terrestrial water systems. In: Turner II, B.L., Clark, W.C., Kates, R.W., Richards, J.F., Mathews, J.T., Meyer, W.B. (Eds.), The Earth as Transformed by Human Action on. Cambridge University Press, Cambridge, UK, pp. 235–252.
McVicar, T.R., Van Niel, T.G., Li, L., King, E.A., Donohue, R.J., 2007. Deriving moisture availability from time series remote sensing for eco-hydrological applications: development of a prototype near real-time operational system. CSIRO Land and Water Science Report, 37/07.
Meyer, W., 1999. Standard reference evaporation calculation for inland, south eastern Australia. Technical report 35/98. CSIRO Land and Water, Adelaide, South Australia.
Miralles, D.G., Gash, G.H., Holmes, T.R.H., de Jeu, R.A.M., Dolman, A.J., 2010. Global canopy interception from satellite observations. J. Geophys. Res. 115, D16122.
Miralles, D.G., Holmes, T.R.H., De Jeu, R.A.M., Gash, J.H., Meesters, A.G.C.A., Dolman, A.J., 2011. Global land-surface evaporation estimated from satellite-based observations. Hydrol. Earth Syst. Sci. 15, 453–469.
Monteith, J.L., 1965. Evaporation and environment. Symp. Soc. Exp. Biol. 19, 205–224.
Mueller, B., Seneviratne, S.I., Jimenez, C., Corti, T., Hirschi, M., Balsamo, G., Ciais, P., Dirmeyer, P., Fisher, J.B., Guo, Z., Jung, M., Maignan, F., McCabe, M.F., Reichle, R., Reichstein, M., Rodell, M., Sheffield, J., Teuling, A.J., Wang, K., Wood, E.F., Zhang, Y., 2011. Evaluation of global observations-based evapotranspiration datasets and IPCC AR4 simulations. Geophys. Res. Lett. 38, L06402.
Mu, Q.Z., Heinsch, F.A., Zhao, M.S., Running, S.W., 2007. Development of a global evapotranspiration algorithm based on MODIS and global meteorology data. Rem. Sens. Environ. 111, 519–536.
Mu, Q.Z., Zhao, M.S., Running, S.W., 2011. Improvements to a MODIS global terrestrial evapotranspiration algorithm. Rem. Sens. Environ. 115, 1781–1800.
Myneni, R.B., Yang, W., Nemani, R.R., Huete, A.R., Dickinson, R.E., Knyazikhin, Y., Didan, K., Fu, R., Negrón Juárez, R.I., Saatchi, S.S., Hashimoto, H., Ichii, K., Shabanov, N.V., Tan, B., Ratana, P., Privette, J.L., Morisette, J.T., Vermote, E.F., Roy, D.P., Wolfe, R.E., Friedl, M.A., Running, S.W., Votava, P., El-Saleous, N., Devadiga, S., Su, Y., Salomonson, V.V., 2007. Large seasonal swings in leaf area of Amazon rainforests. Proc. Natl. Acad. Sci. U. S. A. 104, 4820–4823.
Nemani, R.R., Keeling, C.D., Hashimoto, H., Jolly, W.M., Piper, S.C., Tucker, C.J., Myneni, P.B., Running, S.W., 2003. Climate-driven increases in global terrestrial net primary production from 1982 to 1999. Science 300, 1560–1563.
Nepstad, D.C., de Carvalho, C.R., Davidson, E.A., Jipp, P.H., Lefebvre, P.A., Negreiros, G.H., Da Silva, E.D., Stone, T.A., Trumbore, S.E., Vieira, S., 1994. The role of deep roots in the hydrological and carbon cycles of Amazonian forests and pastures. Nature 372, 666–669.
Norman, J.M., Kustas, W.P., Humes, K.S., 1995. A two-source approach for estimating soil and vegetation energy fluxes in observations of directional radiometric surface temperature. Agric. For. Meteor. 77, 263–293.
Piao, S., Friedlingstein, P., Ciais, P., Ducoudre', N.D.N., Labat, D., Zaehle, S., 2007. Changes in climate and land use have a larger direct impact than rising CO_2 on global river runoff trends. Proc. Natl. Acad. Sci. U.S.A. 104, 242–247.
Pinker, R.T., Zhang, B., Dutton, E.G., 2005. Do satellites detect trends in surface solar radiation? Science 308, 850–854.
Price, J.C., 1985. On the analysis of thermal infrared imagery: the limited utility of apparent thermal inertia. Rem. Sens. Environ. 18, 59–73.
Priestley, C.H.B., Taylor, R.J., 1972. On the assessment of surface heat flux and evaporation using large-scale parameters. Mon. Weather Rev. 100, 81–92.
Qian, W.H., Shan, X.L., Zhu, Y.F., 2011. Ranking regional drought events in China for 1960–2009. Adv. Atmos. Res. 28, 310–321.
Qi, H.X., Zhi, X.F., Bai, Y.Q., 2011. Inter-decadal variation and trend analysis of the drought occurrence frequency in China. Trans. Atmos. Sci. 34, 447–455 (in Chinese).
Raupach, M.R., 2001. Combination theory and equilibrium evaporation. Quart. J. Roy. Meteor. Soc. 127, 1149–1181.
Rouse, W.R., 1984. Microclimate at arctic tree line. The effects of regional advection on the surface energy balance of upland tundra. Water Resour. Res. 20, 74–78.
Sasai, T., Saigusa, N., Nasahara, K.N., Ito, A., Hashimoto, H., Nemani, R., Hirata, R., Ichii, K., Takagi, K., Saitoh, T.M., Ohta, T., Murakami, K., Yamaguchi, Y., Oikawa, T., 2011. Satellite-driven estimation of terrestrial carbon flux over Far East Asia with 1-km grid resolution. Rem. Sens. Environ. 115, 1758–1771.
Schenk, H.J., Jackson, R.B., 2005. Mapping the global distribution of deep roots in relation to climate and soil characteristics. Geoderma 126, 129–140.
Seneviratne, S.I., Corti, T., Davin, E.L., Hirschi, M., Jaeger, E.B., Lehner, I., Orlowsky, B., Teuling, A.J., 2010. Investigating soil moisture–climate interactions in a changing climate: a review. Earth Sci. Rev. 99, 125–161.
Shuttleworth, W.J., Wallace, J.S., 1985. Evaporation from sparse crops an energy combination theory. Quart. J. Roy. Meteor. Soc. 111, 839–855.
Sumner, D.M., Jacobs, J.M., 2005. Utility of Penman–Monteith, Priestley–Taylor, reference evapotranspiration, and pan evaporation methods to estimate pasture evapotranspiration. J. Hydrol. 308, 81–104.
Sun, Y.J., Wang, J.F., Zhang, R.H., Gillies, R.R., Xue, Y., Bo, Y.C., 2005. Air temperature retrieval from remote sensing data based on thermodynamics. Theor. Appl. Climatol. 80, 37–48.
Tang, R.L., Li, Z.L., Tang, B.H., 2010. An application of the Ts-VI triangle method with enhanced edges determination for evapotranspiration estimation from MODIS data in arid and semi-arid regions: implementation and validation. Rem. Sens. Environ. 114, 540–551.
Teuling, A.J., Hirschi, M., Ohmura, A., Wild, M., Reichstein, M., Ciais, P., Buchmann, N., Ammann, C., Montagnani, L., Richardson, A.D., Wohlfahrt, G., Seneviratne, S.I., 2009. A regional perspective on trends in continental evaporation. Geophys. Res. Lett. 36, L02404.
Trenberth, K.E., Fasullo, J., Kiehl, J., 2009. Earth's global energy budget. Bull. Am. Meteorol. Soc. 90, 311–935, 323.
Tucker, C.J., 1979. Red and photographic infrared linear combinations for monitoring. Rem. Sens. Environ. 8, 127–150.
Turner, D.P., Ritts, W.D., Cohen, W.B., Gower, S.T., Zhao, M., Running, S.W., Wofsy, S.C., Urbanski, S., Dunn, A.L., Munger, J.W., 2003. Scaling gross primary production (GPP) over boreal and deciduous forest landscapes in support of MODIS GPP product validation. Rem. Sens. Environ. 88, 256–270.
Twine, T.E., Kustas, W.P., Norman, J.M., Cook, D.R., Houser, P.R., Meyers, T.P., Prueger, J.J., Starks, P.J., Wesely, M.L., 2000. Correcting eddy-covariance flux underestimates over a grassland. Agric. For. Meteorol. 103, 279–300.
Wang, C.Z., Guo, H.D., Zhang, L., Liu, S.Y., Qiu, Y.B., Sun, Z.C., 2012. Quantifying alpine grassland biomass and its climate dependencies in the tibetan plateau with MODIS time series. In: 1st International Symposium on Land Remote Sensing, Chengdu, China, May 30–June 1, pp. 1–23.
Wang, H.S., Jia, G.S., Fu, C.B., Feng, J.M., Zhao, T.B., Mu, Z.G., 2010a. Deriving maximal light use efficiency from coordinated flux measurements and satellite data for regional gross primary production modeling. Rem. Sens. Environ. 114, 2248–2258.
Wang, K.C., Dickinson, R., 2012. A review of global terrestrial evapotranspiration: observation, modeling, climatology, and climatic variability. Rev. Geophys. 50, RG2005.
Wang, K.C., Dickinson, R., Liang, S.L., 2009. Clear sky visibility has decreased over land globally from 1973 to 2007. Science 323, 1468–1470.
Wang, K.C., Dickinson, R., Wild, M., Liang, S.L., 2010b. Evidence for decadal variation in global terrestrial evapotranspiration between 1982 and 2002. Part 1: Model development. J. Geophys. Res. 115, D20112.
Wang, K.C., Dickinson, R., Wild, M., Liang, S.L., 2010c. Evidence for decadal variation in global terrestrial evapotranspiration between 1982 and 2002. Part 2: Results. J. Geophys. Res. 115, D20113.
Wang, K.C., Liang, S.L., 2008. An improved method for estimating global evapotranspiration based on satellite determination of surface net radiation, vegetation index, temperature, and soil moisture. J. Hydrometeorol. 9, 712–727.
Wang, K.C., Wang, P.C., Li, Z.Q., Sparrow, M., 2007. A simple method to estimate actual evapotranspiration from a combination of net radiation, vegetation index, and temperature. J. Geophys. Res. 112, D15107.

Wang, K., Wan, Z., Wang, P., Sparrow, M., Liu, J., Zhou, X., Haginoya, S., 2005. Estimation of surface long wave radiation and broadband emissivity using MODIS land surface temperature/emissivity products. J. Geophys. Res. 110, D11109.

Yang, J., Gong, D.Y., Wang, W.S., Hu, M., Mao, R., 2012. Extreme drought event of 2009/2010 over southwestern China. Meteorol. Atmos. Phys. 115, 173–184.

Yao, Y.J., Qin, Q.M., Ghulam, A., Liu, S.M., Zhao, S.H., Xu, Z.W., Dong, H., 2011a. Simple method to determine the Priestley–Taylor parameter for evapotranspiration estimation using Albedo-VI triangular space from MODIS data. J. Appl. Remote Sens. 5, 053505.

Yao, Y.J., Liang, S.L., Qin, Q.M., Wang, K.C., Zhao, S.H., 2011b. Monitoring global land surface drought based on a hybrid evapotranspiration model. Int. J. Appl. Earth Obs. 13, 447–457.

Yao, Y.J., Liang, S.L., Qin, Q.M., Wang, K.C., Liu, S.M., Zhao, S.H., 2012. Satellite detection of increases in global land surface evapotranspiration during 1984–2007. Int. J. Digit. Earth 5, 299–318.

Yuan, W.P., Liu, S.G., Yu, G.R., Bonnefond, J.M., Chen, J.Q., Davis, K., Desai, A.R., Goldstein, A.H., Gianelle, D., Rossi, F., Suyker, A.E., Verma, S.B., 2010. Global estimates of evapotranspiration and gross primary production based on MODIS and global meteorology data. Rem. Sens. Environ. 114, 1416–1431.

Zakšek, K., Homscheidt, M.S., 2009. Parameterization of air temperature in high temporal and spatial resolution from a combination of the SEVIRI and MODIS instruments. ISPRS J. Photogramm. 64, 414–421.

Zhang, K., Kimball, J.S., Mu, Q.Z., Jones, L.A., Goetz, S.J., Running, S.W., 2009. Satellite based analysis of northern ET trends and associated changes in the regional water balance from 1983 to 2005. J. Hydrol. 379, 92–110.

Zhang, K., Kimball, J.S., Nemani, R.R., Running, S.W., 2010. A continuous satellite-derived global record of land surface evapotranspiration from 1983 to 2006. Water Resour. Res. 46, W09522.

Zhang, R.H., Sun, X.M., Zhu, Z.L., Su, H.B., Tang, X.Z., 2003. A remote sensing model for monitoring soil evaporation based on thermal inertia and its validation. Sci. China Ser. D 46, 342–355.

Zhang, Y.Q., Chiew, F.H.S., Zhang, L., Leuning, R., Cleugh, H.A., 2008. Estimating catchment evaporation and runoff using MODIS leaf area index and the Penman–Monteith equation. Water Resour. Res. 44 (10), W10420.

Zhao, M., Heinsch, F.A., Nemani, R., Running, S.W., 2005. Improvements of the MODIS terrestrial gross and net primary production global data set. Rem. Sens. Environ. 95, 164–176.

Zhao, M., Running, S.W., 2010. Drought-induced reduction in global terrestrial net primary production from 2000 through 2009. Science 329, 940–943.

Zheng, X.B., Zhou, C.X., Luo, Y.X., Chen, J., Zhao, T.L., 2011. Chinese province-level variations and trends in aerosol optical depth from recent 10 years of remote sensing data. Ecol. Environ. Sci. 20, 595–599 (in Chinese).

Zhou, L.M., Dickinson, R.E., Tian, Y.H., Fang, J.Y., Li, Q.X., Kaufmann, R.K., Tucker, C.J., Myneni, R.B., 2004. Evidence for a significant urbanization effect on climate in china. Proc. Natl. Acad. Sci. U. S. A. 101, 9540–9544.